A spectral global matrix method for modelling the response of a fluid-loaded multilayered cylindrical shell excited by an acoustic plane wave

Maxime Dana, Julien Julien Bernard, Laurent Maxit

To cite this version:

Maxime Dana, Julien Julien Bernard, Laurent Maxit. A spectral global matrix method for modelling the response of a fluid-loaded multilayered cylindrical shell excited by an acoustic plane wave. Journal of the Acoustical Society of America, 2020, 148 (5), pp.2997-3013. 10.1121/10.0002353 . hal-03025304

HAL Id: hal-03025304
https://hal.science/hal-03025304

Submitted on 26 Nov 2020

A spectral global matrix method for modelling the response of a fluid-loaded multilayered cylindrical shell excited by an acoustic plane wave

Maxime DANA,[1, a] Julien BERNARD,[2] and Laurent MAXIT[1]

[1] *Univ Lyon, INSA-Lyon, LVA EA677, 25 bis avenue Jean Capelle, F-69621 Villeurbanne Cedex, France*

[2] *Thales Underwater Systems, 525 route des Dolines F-06560 Valbonne, France*

(Dated: 25 November 2020)

This paper proposes a numerically stable method for modelling a fluid-loaded multilayered cylindrical shell excited by a plane wave, which solves the fd instability problem usually observed when using the well known transfer matrix method. In the considered modelling, each layer can be either a viscoelastic coating described by a general 3D elasticity model or an intermediate perfect fluid layer. The transfer matrix of each layer relating the state-vector at the layer's two interfaces is estimated with an appropriate standard method. Instead to multiply together the layer transfer matrices in order to deduce the one of the multilayer cylinder, one writes the continuity relations at each interface of the considered systems yielding to build a global matrix that can be solved to obtain the system response. As shown by numerical applications on typical naval test cases, the proposed global matrix assembly procedure as opposed to the classical transfer matrix method provides both numerical stability over a wide range of axial wavenumbers and circumferential orders, but also the ability of considering intermediate fluid layers. Besides, this model is well-suited to describe elastic solid layers of any anisotropy as illustrated by an additional case considering a transverse isotropic layer.

---

[a] maxime.dana1@gmail.com

I. INTRODUCTION

Underwater vehicles generally include by a cylindrical shell and internal ring stiffeners made of metal to resist to the hydrostatic pressure. The cylindrical shell may be coated with viscoelastic layers to improve the vehicle acoustic stealth. Additionnaly sonar systems may be mounted on the shell to provide for acoustic detection of other underwater and surface vehicles. These sonar systems typically include several elastic and viscoelastic layers to ensure sensor encapsulation, positionning, signal conditionning, and self noise rejection. Incoming signals from remote vehicles is usually modeled as an incident plane wave. At frequencies of interest of most sonar systems, the response of the embedded sensors to a plane wave excitation only involves the local characteristics of the shell. Therefore the vehicle may be modeled as an infinite cyclindrical multilayer system made of elastic, viscoelastic, and fluid layers, without loss of accuracy. In the present paper, the ring stiffeners are not considered but the presented model can be coupled to stiffener models subsequently.

Numerous works have been carried out to model the acoustic scattering and radiation of multilayered plates or cylinders (see for instance (Hull and Welch, 2010; Schmidt and Jensen, 1985) for planar geometries and (Baron, 2011; Ricks and Schmidt, 1994) for cylindrical geometries). For these ideal geometries, exact analytical methods have been developed to save computing times compared to general element-based methods like Finite Element Method and Boundary Element Method. The use of the 3-D equations of elastodynamics appears as the most relevant way of modeling the layers at high wavenumber-thickness product (kd), that is when layer thickness becomes large compared to structural wavelength.

However, specific problems and numerical instabilities can be encountered when considering the cylindrical geometry.

Actually, the step of integrating the displacement solution field in each layer is far less complex in the plane case than in the cylindrical case, since the equations of motion leads to a 2nd order differential system with *constant* matrix coefficients for the displacement field solution. It is not the case for cylindrical geometries for which the matrix coefficients are dependent on the radius position. Two different types of approach have been proposed to overcome this difficulty:

1. The use of Helmholtz decomposition allows to integrate the 2nd order differential system for the displacement field, but restrains the complexity of the considered layer to the elastic isotropic case (Ricks and Schmidt, 1994; Skelton and James, 1997). Even if the generality of this formalism can be extended to a particular case of transverse isotropy (Honarvar *et al.*, 2007; Kim and Ih, 2003; Niklasson and Datta, 1998), the direction of the fibers' material which can be represented is not of interest for the design of the acoustic coatings used in underwater vehicles. Moreover, the introduction of Bessel functions raises numerical problems which must be dealt with, due to the great dynamic range of these mathematical functions (Abramowitz and Stegun, 1965).

2. The state space approach rearranges equations of motion, Cauchy relation and Hooke's law into a 1st order differential system based on sextic Stroh's formalism, whose hybrid solution contains both displacement and normal stress field (Baron, 2011; Chen *et al.*, 2004; Dutrion, 2014; Hasheminejad and Rajabi, 2007; Jamali *et al.*, 2011).

   This approach allows to adress also the problem of elastic anisotropy, either by expanding the matricant solution into a Peano series' decomposition (Baron, 2005, 2011), or by substructuring each layer into a certain number of sublayers fine enough to neglect the curvature inside each sublayer. The latter integration method is most prevalent and is chosen by many authors (Chen *et al.*, 2004; Dutrion, 2014; Hasheminejad and Rajabi, 2007; Jamali *et al.*, 2011).

However, sextic Stroh's formalism establishes transfer matrices in each layer for which the classical assembly procedure is to propagate the displacement-stress field by matrix product. This assembly procedure is generally called the "transfer matrix method" (TMM) and has been used by many authors (see for instance(Chen *et al.*, 2004; Hasheminejad and Rajabi, 2007; Jamali *et al.*, 2011)). However, this one suffers from great instability at high kd, well-known as the "large fd problem" and first pointed by Dunkin (Dunkin, 1965). Even if many authors tried to solve these instabilities by improving the propagation scheme (Dunkin, 1965; Lévesque and Piché, 1992; Rokhlin and Wang, 2002; Tan, 2005), more stable results have been found when a global matrix assembly procedure is chosen (Ricks and Schmidt, 1994; Schmidt and Jensen, 1985). However, this is achieved at the expense of generality for the behavior of the solid layers, since it is assumed isotropic.

Besides, the incompatibility between transfer matrices of solid and fluid layers makes it difficult to take into account intermediate fluid layers. One way of dealing with the problem is to ensure the consistency of the matrix product, either by condensating the transfer matrices in solid layers (Cervenka and Challande, 1991) or by introducing an infinitesimal shear velocity in the fluid medium then considering it as a solid layer (Lowe, 1995; Pialucha, 1992). An other approach is to uncouple shear stresses between the two layers of different nature via an intermediate matrix (Nayfeh and Taylor, 1988; Pilarski, 1985).

In this present paper, we propose to develop an alternative approach for modelling the multilayered shell that circumvents the drawbacks described previously with the existing method (i.e. material restriction for the Helmholtz decomposition, "large fd problem" and incompatibility of the intermediate fluid layers' transfer matrices for the sextic Stroh's formalism when followed by the transfer matrix method). This approach is based on the integration of the displacement-stress field solution of sextic Stroh's formalism to deduce the transfer matrix for each layer of the considered system. However, instead to propagate the state vectors by matrix product, a global matrix assembly procedure is proposed. This approach is similar to that used by authors considering Helmholtz decomposition within each layer, but here it is applied to the sextic Stroh's formalism. This global matrix is built such that the continuity relations at the interfaces of the different layers are satisfied.

This approach is specifically developed such that the broadband analysis can be carried out without suffering numerical singularities at high frequencies, large radiuses of the shell or high thicknesses of the layers. Unlike models that favor Helmholtz decomposition for integrating the solution inside each elementary layer (Ricks and Schmidt, 1994; Skelton and James, 1997), the proposed one is well suited for describing the full anisotropy problem.

To address the problem of interest for underwater applications, multilayered cylindrical shells will be loaded both by internal and external fluids and will be excited by an incoming acoustic plane wave excitation. The steel cylindrical shell and the acoustic coating will be modelled with three-dimensional fully elastic solids, whereas internal, external and intermediate fluid layers are modelled as three-dimensional fluid domains.

The paper is organized as follow:

- In Sec. 2, we remind some theoretical contents related to the considered problem: first, the sextic Stroh's formalism consisting in rearranging the equations of motion, Cauchy relation and Hooke's law, is presented; Second, the 1$^{\text{st}}$ order differential system resulting of the sextic Stroh's formalism is integrated after partitioning each layer into several sublayers fine enough to neglect the curvature of the layer. Last, the classical assembly procedure (generally named "transfer matrix method") is presented to estimate the transfer matrix of either a given layer from that of its constitutive sublayers either or the whole multilayered cylindrical shell from the ones of the different layers;

- In Sec. 3, we highlight both kinds of singularities related to the classical assembly procedure (i.e. "large fd problem" and the management of intermediate fluid layers) on various underwater configurations. To end, the response of the immerged multilayered shell excited by a plane wave is computed. It is compared to that obtained from a numerically robust model limited to isotropic solid layers, and similar to the Direct Global Method (DGM) presented by Ricks (Ricks and Schmidt, 1994) in 1994;

- In Sec. 4, we describe the proposed assembly procedure that allows to overcome the numerical issues presenting previously. The performances of the improved algorithm are studied on the configurations considered in Sec. 3;

- Before concluding, we highlight in Sec. 5 the ability of the developed approach to take into account non-isotropic layers. The case of a shell covered by an transversely isotropic layer composed by Glass Reinforced Plastic is considered.

II. SEXTIC STROH'S FORMALISM AND CLASSICAL MATRIX PRODUCT ASSEMBLY

A. Description of the model

An infinite thick multilayered cylindrical structure (MCS) of N layers is centred on its z axis as shown in Fig. 1a). The radial, circumferential and axial coordinates are respectively denoted by r, ϕ and z whereas its associated unit vectors are respectively mentioned by $\boldsymbol{e}_r$, $\boldsymbol{e}_\phi$ and $\boldsymbol{e}_z$. Each layer is composed either by an homogeneous elastic material or by a perfect fluid. As described in Fig. 1b), the j^{th} layer $j \in [1, N]$ is delimited by its extremal radiuses r_{j-1} and r_j (with $r_{j-1} < r_j$). It results that r_0 and r_{N} denote respectively the internal and external radiuses of the MCS. The inner cavity of the MCS is supposed to be filled by air whereas the MCS is assumed to be immersed in water. By convention, the 0^{th} and $\mathrm{N}+1^{\text{th}}$ layers respectively denote the internal air cavity and the external water domain.

An incoming acoustic plane wave in the external medium is considered as the only excitation exerted on the MCS, apart from the fluid couplings. The harmonic time dependence is chosen as $e^{-j\omega t}$ and will be suppressed throughout this paper as an algebraic convention.

We will develop a model for predicting the vibroacoustic response of the MCS excited by the plane wave. The latter will be characterised by the response at a given receiving point that can be placed either in the external fluid or embedded within an arbitrary layer of the MCS. The reponse for the point located in a fluid medium (i.e. external fluid or intermediate fluid layer) will be the acoustic pressure whereas for the point located in a solid layer, it will be the radial stress. The point of interest will be located at the position coordinates (r_A, ϕ_A, z_A).

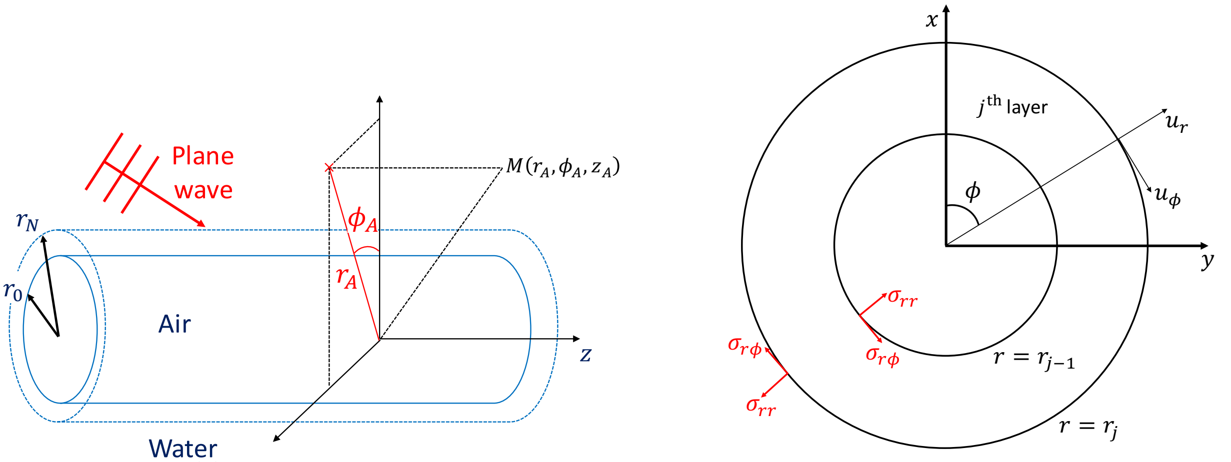

(a) Multilayered shell (b) Sectional view of the j^{th} layer in the $x - y$ plane

FIG. 1. Presentation of the multilayered shell impacted by an acoustic plane wave

B. 3D anisotropic elasticity and state equation

In 2004, Chen & al. (Chen *et al.*, 2004) derived a sixth-order state equation for a general anisotropic medium in cylindrical coordinates from the 3-dimensional fundamental equations of anisotropic elasticity. Here, one considers a particular case of their developments when no body forces nor thermal effect are taken into account.

This formalism rests on the assumption of infinitesimal strain theory in any j^{th} layer, and the rearrangement of equations of motion, Cauchy relation and Hooke's law. Let us consider the state vector defined by:

$$\boldsymbol{V} = \begin{bmatrix} u_z & u_\phi & u_r & \sigma_{rr} & \sigma_{r\phi} & \sigma_{rz} \end{bmatrix}^T \tag{1}$$

where $\boldsymbol{u}$ and $\boldsymbol{\sigma}$ represent the displacement and the stress, respectively.

After algebraic manipulations of the previously named equations (see (Chen *et al.*, 2004)), one can obtain the so-called state equation for any anisotropic solid layer j (index j is omitted on purpose):

$$\frac{\partial \boldsymbol{V}}{\partial r}(r, \phi, z) = [\boldsymbol{\mathcal{Q}}]\, \boldsymbol{V}(r, \phi, z) \tag{2}$$

where $[\boldsymbol{\mathcal{Q}}]$ is the Stroh's operator being dependent on the elastic constants of the considered layer (Chen *et al.*, 2004).

For the sake of brevity and clarity, in the following one only considers the orthotropic elastic materials although the presented numerical process could be also applied to any anisotropic material. In the specific orthotropic case, the stiffness tensor shows only 9 independent elastic constants and Hooke's law takes the expression (47) given in Appendix.

Thus, for this case, the $[\boldsymbol{\mathcal{Q}}]$ Stroh's operator reduces to (48) given once again in Appendix.

C. Fourier transforms and Stroh's differential system

Operator $[\boldsymbol{\mathcal{Q}}]$ in equation (2) includes partial derivatives along the circumferential and axial directions which make the integration of the solution not immediately tractable. Thus, the field quantities are represented by Fourier integral transforms in the axial direction and Fourier series transforms in the circumferential direction. Actually, any $F(r, \phi, z)$ physical field in the cylindrical coordinate system can be expressed as

$$F(r,\phi,z)=\frac{1}{2\pi}\sum_{n=-\infty}^{+\infty}e^{in\phi}\int_{-\infty}^{+\infty}\tilde{F}(r,n,\alpha)e^{i\alpha z}d\alpha \tag{3}$$

where the associated spectral quantity $\tilde{F}(r,n,\alpha)$ is given by the Fourier transform:

$$\tilde{F}(r,n,\alpha)=\frac{1}{2\pi}\int_{0}^{2\pi}e^{-in\phi}\int_{-\infty}^{+\infty}F(r,\phi,z)e^{-i\alpha z}dzd\phi \tag{4}$$

Solving equation (2) in the spectral domain by using Fourier transforms allows us to reduce the linear partial differential equations in the variables (r,ϕ,z) into ordinary differential equations in the radial variable r. Hence, equation (2) and the Stroh's matrix $[\boldsymbol{\mathcal{Q}}]$ for the orthotropic case become in the spectral domain:

$$\frac{d\tilde{\boldsymbol{V}}}{dr}(r,n,\alpha)=[\boldsymbol{Q}(r)]\,\tilde{\boldsymbol{V}}(r,n,\alpha) \tag{5}$$

The latter equation is a 1$^{\text{st}}$ order differential system for the radial variable r, in which the matrix $[\boldsymbol{Q}(r)]$ is given by (50) in Appendix and is also dependent of the radial coordinate. This is the main reason why the derived system differs from the one obtained in cartesian coordinates for plane layers, and why the solution is not directly integrable in the same way. However, the decomposition of the layer in thin sublayers will allow us to neglect locally the effect of the curvature of the cylindrical sublayer and to approximate the matrix $[\boldsymbol{Q}(r)]$ as a constant in the equation system (5) for each thin sublayer. This approach is described in the following subsection.

D. Transfer matrices

1. Case of an elastic solid layer

Let us consider a solid layer partitioned into P different sublayers of equal thickness as represented in Fig. 2.

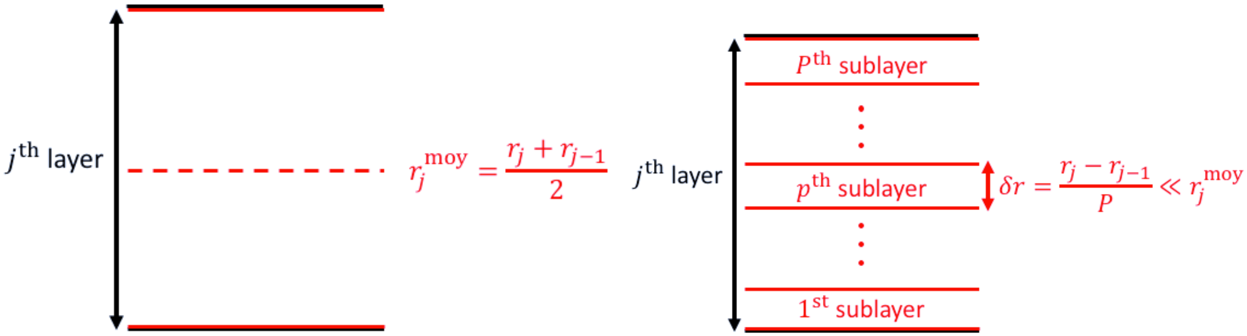

(a) Mean radius of j^{th} layer (b) Substructuring criteria of j^{th} layer

FIG. 2. Substructuring approach for the integration of the Stroh's system

Its extremal radiuses and mean radius are noted respectively r_{j-1}, r_j and $r_j^{\text{moy}} = \frac{r_j + r_{j-1}}{2}$. Each sublayer has a constant thickness $\delta r = \frac{r_j - r_{j-1}}{P}$ which is assumed much lower than the mean radius (i.e. typically $\frac{\delta r}{r_j^{\text{moy}}} \leq 0.1$) in order to neglect the curvature locally inside each sublayer. The sublayer p of the j^{th} layer is then delimited between its extremal radiuses $r_{j,p}^{\text{inf}}$ and $r_{j,p}^{\text{sup}}$, and its mean radius is noted $r_{j,p}^{\text{moy}}$. These geometrical parameters verify for $p \in [1, P]$:

$$r_{j,p}^{\text{inf}} = r_{j-1} + (p-1)\,\delta r, \quad r_{j,p}^{\text{moy}} = r_{j,p}^{\text{inf}} + \frac{\delta r}{2}, \quad r_{j,p}^{\text{sup}} = r_{j,p}^{\text{inf}} + \delta r \tag{6}$$

Inside each sublayer p of the j^{th} layer, the state vector $\boldsymbol{V}_j^p$ is the solution of a Stroh's system only valid along the thickness δr. As this latter parameter is assumed small compared to the mean radius, one can approximate the Stroh's matrix by its value at mean radius $r_{j,p}^{\text{moy}}$:

$$\begin{aligned} &\frac{d\tilde{\boldsymbol{V}}_j^p}{dr}(r,n,\alpha) = \left[\boldsymbol{Q}_j^p(r_{j,p}^{\text{moy}})\right]\tilde{\boldsymbol{V}}_j^p(r,n,\alpha),\ \forall r\in[r_{j,p}^{\text{inf}}, r_{j,p}^{\text{sup}}] \\ &\tilde{\boldsymbol{V}}_j^p(r_{j,p}^{\text{inf}},n,\alpha) = \tilde{\boldsymbol{V}}_{j,0}^p \end{aligned} \tag{7}$$

According to Picard-Lindelöf's theorem, uniqueness of previous system (7) is ensured by the initial data of the state vector at the inferior interface of the sublayer which is noted $\tilde{\boldsymbol{V}}_{j,0}^p$. Besides, operator $\left[\boldsymbol{Q}_j^p(r_{j,p}^{\text{moy}})\right]$ in Eq. (7) is assumed constant across the entire thickness δr of the sublayer, and is evaluated at its mean radius $r_{j,p}^{\text{moy}}$. The solution is expressed with a matrix exponential as:

$$\boldsymbol{V}_j^p(r,n,\alpha) = e^{\left(r-r_{j,p}^{\text{inf}}\right)\left[\boldsymbol{Q}_j^p(r_{j,p}^{\text{moy}})\right]}\boldsymbol{V}_{j,0}^p \tag{8}$$

The transfer matrix of the sublayer p is defined as the matrix that relates the state vector at the inferior radius to the one at the superior radius of the sublayer p. Eq. (8) evaluated for $r = r_{j,p}^{\text{sup}}$ enables to establish this transfer matrix noted $[\boldsymbol{T}_j]^p$:

$$\begin{gathered} \tilde{\boldsymbol{V}}_j^p(r_{j,p}^{\text{sup}},n,\alpha) = [\boldsymbol{T}_j]^p\,\tilde{\boldsymbol{V}}_j^p(r_{j,p}^{\text{inf}},n,\alpha) \\ \text{with } [\boldsymbol{T}_j]^p = e^{\left(r_{j,p}^{\text{sup}}-r_{j,p}^{\text{inf}}\right)\left[\boldsymbol{Q}_j^p(r_{j,p}^{\text{moy}})\right]} \end{gathered} \tag{9}$$

2. Case of an acoustic fluid layer

Let us consider an acoustic fluid layer j. Only the acoustic pressure p_a and the radial displacement u_a are the components of the state vector $\boldsymbol{V}_j = \begin{bmatrix} u_a & p_a \end{bmatrix}^T$. Considering the Fourier transforms of the acoustic wave equation, one can deduce its solutions in terms of Bessel functions. It can then be shown (Ricks and Schmidt, 1994) that the 2×1 spectral state vectors at both extremal interfaces of the fluid layer j can be related by a 2×2 transfer matrix as:

$$\begin{aligned}\tilde{\boldsymbol{V}}_j(r_j,n,\alpha) &= [\boldsymbol{T}]_j\,\tilde{\boldsymbol{V}}_j(r_{j-1},n,\alpha)\\ \text{with}\,[\boldsymbol{T}]_j &= [\boldsymbol{F}(r_j,n,\alpha)]\,[\boldsymbol{F}(r_{j-1},n,\alpha)]^{-1}\end{aligned} \tag{10}$$

where $[\boldsymbol{F}(r,n,\alpha)]$ is called the elementary fluid matrix, and has the following coefficients:

$$[\boldsymbol{F}(r,n,\alpha)] = \begin{bmatrix} \gamma_L J_n'(\gamma_L r) & \gamma_L H_n^{(1)'}(\gamma_L r) \\ -\rho\omega^2 J_n(\gamma_L r) & -\rho\omega^2 H_n^{(1)}(\gamma_L r) \end{bmatrix} \tag{11}$$

where J_n and $H_n^{(1)}$ are respectively Bessel and Hankel functions of the first kind. These functions are evaluated at $\gamma_L r$, where $\gamma_L = \sqrt{k_L^2 - \alpha^2}$ is the projected wavenumber along the radial coordinate, $k_L = \dfrac{\omega}{c_L}$ is the acoustic wavenumber in the considered fluid, and c_L and ρ are respectively the sound velocity and the mass density in this same medium.

E. Classical matrix product assembly: the Transfer Matrix Method (TMM)

This section presents the classical assembly procedure of the different layers of the structure which leads to numerical singularities as we will see in Sec. 3. It is based on the writing of a matrix product which expresses implicitly the continuity relations at each interface between state vectors of two consecutive layers. This approach can be applied indifferently to the transfer matrices of the sublayers of a given layer to obtain its transfer matrix or to the transfer matrices of the different layers of the MCS to obtain the global transfer matrix of the MCS.

It has to be noted than when the structure has intermediate fluid layers, a condensation of the state vector is required as the state vectors of the structure layers have 6 components whereas there are only 2 for the fluid layers. The following sections presents first the case with no condensation and then the case with condensation.

1. Without intermediate fluid layers

When no fluid layers are considered in the structure, consistency in the matrix product is obtained naturally between all elastic solid layers.

a. Case 1: Assembly of sublayers to calculate the transfer matrix of the considered layer. In Sec. 2.4.1., the elastic solid layer j has been partitioned in P fictive sublayers and the transfer matrix of each sublayer has been determined by Eq. (9). At the interface between each sublayer, the displacement continuity and the force equilibrium should be fulfilled. Actually, for any given sublayers $p-1$ and p, $p \in [\![2;P]\!]$, one has at the shared interface of equation $r = r_{j,p}^{\text{inf}} = r_{j,p-1}^{\text{sup}}$:

$$\forall p \in [\![2;P]\!], \boldsymbol{V}_j^p(r_{j,p}^{\text{inf}}, n, \alpha) = \boldsymbol{V}_j^{p-1}(r_{j,p-1}^{\text{sup}}, n, \alpha) \tag{12}$$

Hence, the transfer matrix for the j^{th} layer is built as the product of the different sublayer transfer matrices, given that the state vector may be propagated across the entire thickness of the layer:

$$\boldsymbol{V}_j^P(r_{j,P}^{\text{sup}}, n, \alpha) = \prod_{p=1}^{P} [\boldsymbol{T}_j]^{P+1-p} \, \boldsymbol{V}_1^1(r_{j,1}^{\text{inf}}, n, \alpha) \tag{13}$$

By identifying that $r_{j,1}^{\text{inf}} = r_{j-1}$ and $r_{j,P}^{\text{sup}} = r_j$, the transfer matrix for the j^{th} layer is easily recognizable:

$$\boldsymbol{V}_j(r_j, n, \alpha) = [\boldsymbol{T}]_j \, \boldsymbol{V}_j(r_{j-1}, n, \alpha), \text{ with } \quad [\boldsymbol{T}]_j = \prod_{p=1}^{P} [\boldsymbol{T}_j]^{P+1-p} \tag{14}$$

b. Case 2: Assembly of layers to calculate the transfer matrix of the multilayered cylindrical shell.

For interfaces separating two consecutive elastic solid layers, the same principle can be applied, assuming a rigid junction between the two layers. Thus, by considering the $j+1^{\text{th}}$ interface separating the layers j and $j+1$ connected at $r = r_j$, we have:

$$\boldsymbol{V}_j(r_j, n, \alpha) = \boldsymbol{V}_{j+1}(r_j, n, \alpha) \tag{15}$$

Propagating the displacement and stress fields across the physical layers is then achieved the same way as across the different sublayers of a given material, and a global transfer matrix $[\boldsymbol{T}]_{\text{struc}}$ for the whole multilayered structure can be defined:

$$\boldsymbol{V}_{\mathrm{N}}(r_{\mathrm{N}}, n, \alpha) = [\boldsymbol{T}]_{\text{struc}}\, \boldsymbol{V}_1(r_0, n, \alpha), \quad [\boldsymbol{T}]_{\text{struc}} = \prod_{j=1}^{N} [\boldsymbol{T}]_{N+1-j} \tag{16}$$

2. ***With at least one intermediate fluid layer***

In the case where the MCS presents at least one intermediate fluid layer, one notes n_f the number of intermediate fluid layers. This implies that the number of *groups* of solid layers is $n_f + 1$, a group being a stack of elastic solid layers framed by two fluid layers. Let us consider now a specific group g of elastic solid layers separated by two fluid layers at its lower and upper interfaces, noted respectively r_g^{lower} and r_g^{upper}. Then state vectors at both sides of fluid-solid interfaces are no longer consistent, and we define for the group of elastic solid layers a reduced state vector $\boldsymbol{V}_g^r = \begin{bmatrix} u_r^g & \sigma_{rr}^g \end{bmatrix}^T$ which contains the radial (i.e. normal to the interface) displacement and the radial stress evaluated at any radial coordinate of the multilayered system, giving for the full state vector the following form:

$$\boldsymbol{V} = \begin{bmatrix} u_z^g & u_\phi^g & \boldsymbol{V}_g^r & \sigma_{r\phi}^g & \sigma_{rz}^g \end{bmatrix}^T \tag{17}$$

Hence, the continuity relation is only about normal displacement and normal stress, and entails nullity of shear stresses. For the upper interface of the solid group, this leads to:

$$\begin{gathered} \boldsymbol{V}_g^r(r_g^{\text{upper}}, n, \alpha) = \boldsymbol{V}_{g+1}^r(r_g^{\text{upper}}, n, \alpha) \\ \begin{bmatrix} \sigma_{r\phi} & \sigma_{rz} \end{bmatrix}^T (r_g^{\text{upper}}, n, \alpha) = \mathbf{0}_2 \end{gathered} \tag{18}$$

and the same goes for the lower interface.

A usual way for dealing with the latter continuity relations consists in condensing the transfer matrix of the group of solid layers.

The g^{th} solid group's transfer matrix $[\boldsymbol{T}]_{\text{g}}$, obtained by matrix product of the transfer matrices of each layer of the group, can be partitioned in 2×2 blocks as follows:

$$\begin{pmatrix} \begin{pmatrix} u_z^g \\ u_\phi^g \end{pmatrix} \\ \boldsymbol{V}_g^r \\ \begin{pmatrix} 0 \\ 0 \end{pmatrix} \end{pmatrix} (r_g^{\text{upper}}, n, \alpha) = \begin{pmatrix} [\boldsymbol{T}_{11}]_g & [\boldsymbol{T}_{12}]_g & [\boldsymbol{T}_{13}]_g \\ [\boldsymbol{T}_{21}]_g & [\boldsymbol{T}_{22}]_g & [\boldsymbol{T}_{23}]_g \\ [\boldsymbol{T}_{31}]_g & [\boldsymbol{T}_{32}]_g & [\boldsymbol{T}_{33}]_g \end{pmatrix} \begin{pmatrix} \begin{pmatrix} u_z^g \\ u_\phi^g \end{pmatrix} \\ \boldsymbol{V}_g^r \\ \begin{pmatrix} 0 \\ 0 \end{pmatrix} \end{pmatrix} (r_g^{\text{lower}}, n, \alpha) \tag{19}$$

The last four equations of system (19) give the following 2×1 equations:

$$\begin{cases} \boldsymbol{V}_g^r(r_g^{\text{upper}}, n, \alpha) = [\boldsymbol{T}_{21}]_g \begin{pmatrix} u_z^g \\ \\ u_\phi^g \end{pmatrix}\Bigg|_{(r_g^{\text{lower}}, n, \alpha)} + [\boldsymbol{T}_{22}]_g \, \boldsymbol{V}_g^r(r_g^{\text{lower}}, n, \alpha) \\ \begin{pmatrix} 0 \\ \\ 0 \end{pmatrix} = [\boldsymbol{T}_{31}]_g \begin{pmatrix} u_z^g \\ \\ u_\phi^g \end{pmatrix}\Bigg|_{(r_g^{\text{lower}}, n, \alpha)} + [\boldsymbol{T}_{32}]_g \, \boldsymbol{V}^r(r_g^{\text{lower}}, n, \alpha) \end{cases} \tag{20}$$

By rearranging the set of equations (20) and eliminating the axial and circumferential displacements, one can establish a *reduced* transfer matrix which propagates the reduced state vector from the lower to the upper interface of g^{th} group:

$$\begin{aligned} \boldsymbol{V}_g^r(r_g^{\text{upper}}, n, \alpha) &= [\boldsymbol{T}]_g^r \, \boldsymbol{V}_g^r(r_g^{\text{lower}}, n, \alpha) \\ \text{with } \ [\boldsymbol{T}]_g^r &= \left[[\boldsymbol{T}_{22}]_g - [\boldsymbol{T}_{21}]_g \, [\boldsymbol{T}_{31}]_g^{-1} \, [\boldsymbol{T}_{32}]_g \right] \end{aligned} \tag{21}$$

Once every group of solid layers has been condensated, one can propagate the reduced state vector across the MCS via the following equation:

$$\boldsymbol{V}_{\text{N}}^r(r_N, n, \alpha) = [\boldsymbol{T}]_{\text{struc}}^r \, \boldsymbol{V}_1^r(r_0, n, \alpha), \quad [\boldsymbol{T}]_{\text{struc}}^r = \prod_{k=1}^{n_f+1} [\boldsymbol{T}]_{n_f+2-k}^r \, [\boldsymbol{T}]_{n_f+2-k}^f \tag{22}$$

where $[\boldsymbol{T}]_k^f$ is the transfer matrix of the intermediate fluid layer framed by the $k-1^{th}$ and k^{th} groups of solid elastic layers.

F. Global calculation and evaluation of the spectral pressure at the receiving point

In the previous section, one has determined the global transfer matrix of the MCS. In order to calculate the global response of the fluid loaded MCS, it is necessary to write the boundary conditions at the internal and external radius of the MCS. In the case of an incident plane wave in the external medium exciting the MCS, the spectral pressure at the external radius r_{N} can be split into the blocked pressure p_b and the scattered pressure p_e (Maxit, 2014):

$$p(r_{\mathrm{N}}, n, \alpha) = p_{\mathrm{b}}(r_{\mathrm{N}}, n, \alpha) + p_e(r_{\mathrm{N}}, n, \alpha). \tag{23}$$

The scattered pressure p_e can be expressed via the external fluid impedance Z_{fe} and the normal displacement at $r = r_{\mathrm{N}}$ of the N^{th} layer of the MCS (after writing the continuity of the normal displacements at the interface between the N^{th} layer and the external fluid):

$$p_e(r_{\mathrm{N}}, n, \alpha) = Z_{\mathrm{fe}} \boldsymbol{u}_{\mathrm{N}}(r_{\mathrm{N}}, n, \alpha) \cdot \boldsymbol{e}_r \tag{24}$$

where $Z_{\mathrm{fe}}(n, \alpha) = \dfrac{\rho_e \omega^2 H_n^{(1)}(\gamma_e r_{\mathrm{N}})}{\gamma_e H_n^{(1)'}(\gamma_e r_{\mathrm{N}})}$, with $\gamma_e = \sqrt{k_e^2 - \alpha^2}$, $k_e = \dfrac{\omega}{c_e}$ being the acoustic wavenumber in the external fluid, and c_e and ρ_e being the sound velocity and the mass density in this same medium.

Supposing that the acoustic wavevector characterizing the incident wave is in the plane $\phi = 0$ and that it makes an angle ψ_i with the axial axis, the blocked pressure induced by the acoustic plane wave can be expressed by (Skelton and James, 1997):

$$p_b(r_{\mathrm{N}}, n, \alpha) = \frac{2\,(-i)^{n+1}}{\pi \gamma_e r_{\mathrm{N}} H_n^{(1)}(\gamma_e r_{\mathrm{N}})} 2\pi \delta\left(\alpha - \alpha^i\right) \tag{25}$$

where $\alpha^i = \cos(\psi_i) k_e$ is the projection of the acoustic wavevector onto the axial axis.

On another hand, the pressure exerted by the internal air cavity can be related to the normal displacement of the first layer at $r = r_0$:

$$p_{1e}(r_0, n, \alpha) = Z_{\mathrm{fi}} \boldsymbol{u}_1(r_0, n, \alpha) \cdot \boldsymbol{e}_r \tag{26}$$

where

$$Z_{\mathrm{fli}}(r, n, \alpha) = \frac{\rho_i \omega^2 J_n(\gamma_i(\alpha) r)}{\gamma_i(\alpha) J_n'(\gamma_i(\alpha) r_0)},$$

with $\gamma_i = \sqrt{k_i^2 - \alpha^2}$, $k_i = \dfrac{\omega}{c_i}$ being the acoustic wavenumber in the external fluid, and c_i and ρ_i being the sound velocity and the mass density in this same medium.

Using a vector-matrix form to be compliant with the transfer matrix, the stress fields applied at the external and internal radiuses on the MCS can be written:

$$\boldsymbol{\sigma}_{\mathrm{N}}(r_{\mathrm{N}}, n, \alpha) = -\boldsymbol{P}_{\mathrm{b}}(r_{\mathrm{N}}, n, \alpha) - [\boldsymbol{T}_{\mathrm{fe}}]\,\boldsymbol{u}_{\mathrm{N}}(r_{\mathrm{N}}, n, \alpha) \tag{27}$$

$$\boldsymbol{\sigma}_1(r_0, n, \alpha) = [\boldsymbol{T}_{\mathrm{fi}}]\,\boldsymbol{u}_1(r_0, n, \alpha) \tag{28}$$

with

$$\boldsymbol{P}_{\mathrm{b}}(r_{\mathrm{N}}, n, \alpha) = p_{\mathrm{b}}(r_{\mathrm{N}}, n, \alpha)\boldsymbol{e}_r$$

$$[\boldsymbol{T}_{\mathrm{fi}}] = \begin{pmatrix} 0 & 0 & 0 \\ 0 & 0 & 0 \\ 0 & 0 & Z_{\mathrm{fi}} \end{pmatrix}, [\boldsymbol{T}_{\mathrm{fe}}] = \begin{pmatrix} 0 & 0 & 0 \\ 0 & 0 & 0 \\ 0 & 0 & Z_{\mathrm{fe}} \end{pmatrix} \tag{29}$$

G. Resolution of the mathematical problem

Considering the transfer matrix of the MCS given by Eq. (16) and the boundary conditions defined by Eq. (27)-(28), one can deduce the displacement and the stress fields of the MCS at the external and internal radiuses.

First, the global transfer matrix is partitioned into 3×3 blocks as follows, in the case where the MCS does not exhibit intermediate fluid layers:

$$\boldsymbol{V}_{\mathrm{N}}(r_{\mathrm{N}}, n, \alpha) = \begin{pmatrix} [\boldsymbol{T}]_{\boldsymbol{u}_{\mathrm{N}}\boldsymbol{u}_1} & [\boldsymbol{T}]_{\boldsymbol{u}_{\mathrm{N}}\boldsymbol{\sigma}_1} \\ [\boldsymbol{T}]_{\boldsymbol{\sigma}_{\mathrm{N}}\boldsymbol{u}_1} & [\boldsymbol{T}]_{\boldsymbol{\sigma}_{\mathrm{N}}\boldsymbol{\sigma}_1} \end{pmatrix} (n, \alpha)\boldsymbol{V}_1(r_0, n, \alpha), \tag{30}$$

where

$$\boldsymbol{V}_{\mathrm{N}} = \begin{bmatrix} \boldsymbol{u}_{\mathrm{N}} & \boldsymbol{\sigma}_{\mathrm{N}} \end{bmatrix}^T \text{ and } \boldsymbol{V}_1 = \begin{bmatrix} \boldsymbol{u}_1 & \boldsymbol{\sigma}_1 \end{bmatrix}^T .$$

Then the displacement field at the internal radius of the MCS can be written:

$$\boldsymbol{u}_1(r_0, n, \alpha) = -\left[\boldsymbol{R}\right]_{\boldsymbol{u}_1 \boldsymbol{F}_{\mathrm{N}}} \boldsymbol{P}_{\mathrm{b}}(r_{\mathrm{N}}, n, \alpha) \tag{31}$$

where

$$\left[\boldsymbol{R}\right]_{\boldsymbol{u}_1 \boldsymbol{F}_N} = \left[\left[\boldsymbol{T}_{\mathrm{fe}}\right]\left[\boldsymbol{T}\right]_{\boldsymbol{u}_{\mathrm{N}} \boldsymbol{u}_1} + \left[\boldsymbol{T}\right]_{\boldsymbol{\sigma}_{\mathrm{N}} \boldsymbol{u}_1} + \left[\left[\boldsymbol{T}\right]_{\boldsymbol{\sigma}_{\mathrm{N}} \boldsymbol{\sigma}_1} + \left[\boldsymbol{T}_{\mathrm{fe}}\right]\left[\boldsymbol{T}\right]_{\boldsymbol{u}_{\mathrm{N}} \boldsymbol{\sigma}_1}\right]\left[\boldsymbol{T}_{\mathrm{fi}}\right]\right]^{-1} \tag{32}$$

An explicit expression for the state vector $\boldsymbol{V}_1 = \begin{bmatrix} \boldsymbol{u}_1 & \boldsymbol{\sigma}_1 \end{bmatrix}^T$ at the internal radius of the MCS can then be established. This state vector can be propagated to the radius of the receiving point using a transfer matrix between the internal radius and the radius of the receiving point. This latter can be estimated by the same way that the global transfer matrix of the MCS has been obtained in Sec. 2.5. From the state vector at the radius of the receiving point expressed in the wavenumber domain (n, α), one can deduce the response at the receiving point by the inverse Fourier transforms (3).

The same way is considered in the case where the structure has at least one intermediate fluid layer. However, as it has been described in Sec. II E 2, only the normal displacement and the normal stress are considered in the reduced matrix transfer. Thus, the latter is partitioned into blocks of four scalar $T^r_{u_{\mathrm{N}} u_1}$, $T^r_{\sigma_{\mathrm{N}} u_1}$, $T^r_{\sigma_{\mathrm{N}} \sigma_1}$ and $T^r_{u_{\mathrm{N}} \sigma_1}$, as follows:

$$\boldsymbol{V}^r_{\mathrm{N}}(r_{\mathrm{N}}, n, \alpha) = \begin{pmatrix} T^r_{u_{\mathrm{N}} u_1} & T^r_{u_{\mathrm{N}} \sigma_1} \\ T^r_{\sigma_{\mathrm{N}} u_1} & T^r_{\sigma_{\mathrm{N}} \sigma_1} \end{pmatrix} (n, \alpha) \boldsymbol{V}^r_1(r_0, n, \alpha), \tag{33}$$

where

$$\boldsymbol{V}^r_{\mathrm{N}} = \begin{bmatrix} u_{\mathrm{N}} & \sigma_{\mathrm{N}} \end{bmatrix}^T \text{ and } \boldsymbol{V}^r_1 = \begin{bmatrix} u_1 & \sigma_1 \end{bmatrix}^T .$$

Finally, the normal displacement at the internal radius can be written:

$$u_1(r_0, n, \alpha) \cdot \boldsymbol{e}_r = -R_{u_1 \boldsymbol{F}_\mathrm{N}} p_\mathrm{b}(r_\mathrm{N}, n, \alpha) \tag{34}$$

with

$$R_{u_1 \boldsymbol{F}_N} = \frac{1}{Z_\mathrm{fe} T^r_{u_\mathrm{N} u_1} + T^r_{\sigma_\mathrm{N} u_1} + \left[T^r_{\sigma_\mathrm{N} \sigma_1} + Z_\mathrm{fe} T^r_{u_\mathrm{N} \sigma_1}\right] Z_\mathrm{fi}}. \tag{35}$$

III. NUMERICAL CONVERGENCE OF THE TMM APPROACH

A. Validation test cases

In this section, we are going to highlight some numerical instabilities of the classical assembly procedure described previously. Numerical singularities compared to a reference are going to be shown on test cases related to underwater applications. In the section 4, we will propose an alternative assembly procedure avoiding these instabilities. Let us consider the four different multilayered cylindrical structures shown on Fig. 3.

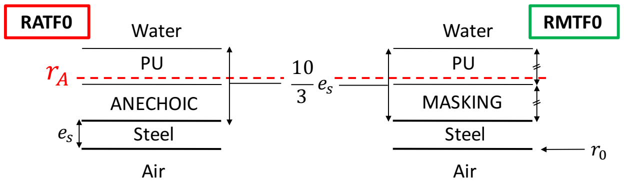

(a) Configurations without acoustic windows (**RATF0** and **RMTF0**)

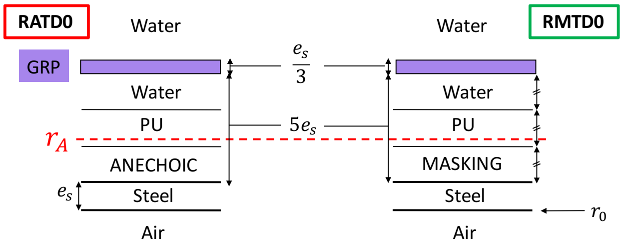

(b) Configurations with acoustic windows (**RATD0** and **RMTD0**)

FIG. 3. Schematic representation of the multilayered cross-section of the different test cases

- the **RATF0** configuration corresponds to a cylindrical steel shell of thickness e_s and of internal radius r_0 covered by an acoustic coating composed by a layer of anechoic material and a layer of polyurethane (PU);

- the **RMTF0** configuration is similar to the **RATF0** at the difference that the anechoic material is replaced by a masking material;

- the **RATD0** and **RMTD0** configurations correspond to **RATF0** and **RMTF0**, respectively, with a supplementary layer of glass reinforced polymer material (GRP) at a given distance of the outer surface of the PU layer. It results in an intermediate layer of water between the PU and GRP layer. For an application point of view, this supplementary GRP layer may represent the acoustic window used in a Sonar flank array to keep the sensors away from the turbulent flow. In this section, the GRP material is assumed isotropic to allow us to obtain a reference result with the Helmholtz decomposition (Ricks and Schmidt, 1994).

For these 4 configurations, the MCS is immersed in water and the internal cavity is filled with air. The MCS is excited by an acoustic plane wave of magnitude A_0. The mechanical properties of the different materials and the ratios of the layer thicknesses to the steel shell thickness e/e_s are shown in Table I.

TABLE I. Material properties. Every solid material is assumed isotropic.

	Steel	PU	ANECHOIC	MASKING	Water	GRP (assumed isotropic)
c_L (m.s^{-1})	6020	1600	900	300	1500	3000
η_L	$0,01$	$0,02$	$0,25$	$0,25$	0	$0,05$
c_T (m.s^{-1})	3220	150	150	100	0	2000
η_T	$0,01$	$0,1$	$0,35$	$0,45$	0	$0,1$
ρ (kg.m^{-3})	7800	1100	1400	1100	1000	2000
e/e_s	1	$\frac{5}{3}$	$\frac{5}{3}$	$\frac{5}{3}$	$\frac{5}{3}$	$\frac{1}{3}$

The calculations will be carried out for a receiving point located at a radius $r_A = r_0 + \frac{10}{3}e_s$. This receiving point is inside the PU layer mimicking an hydrophone sensor embedded in the PU of a Sonar. The response at this point will be evaluated in term of the radial stress σ_{rr}.

The TMM calculations have been performed as described in the section 2. The material properties are used to evaluate the Stroh's matrix (Eq. (5)) reminding that the stiffness constants are related to the longitudinal and transverse velocities by: $c_{11} = c_{22} = c_{33} = \rho c_L^2, c_{44} = c_{55} = c_{66} = \rho c_T^2$ and $c_{12} = c_{13} = c_{23} = \rho(c_L^2 - 2c_T^2)$. As detailed in the section II D 1, the layer can be decomposed in several sublayers in order to suppose that the Stroh's matrix is independent on the radius in the sublayer. Calculations considering different numbers of sublayers for each layer were carried out and they showed very close results even when considering one single sublayer. One concludes that for the considered configurations and the considered frequency range of interest, it is not necessary to decompose the layers in different sublayers. This is due to the fact that the criterion $\dfrac{\delta r}{r_j^{\text{moy}}} \leq 0.1$ is sufficiently respected for the considered cases. In the following subsections, the obtained TMM results are going to be compared to the reference results obtained with the so called Dynamic Global Method based on Helmholtz Decomposition (DGM-HD). This latter is based on the DGM method introduced by Ricks in 1994 (Ricks and Schmidt, 1994), namely a Helmholtz decomposition performed in each elementary layer, followed by a global matrix assembly procedure. The DGM-HD calculations have been previously validated by comparison with other models, in particular finite element models. We can underline that the TMM and DGM-HD approaches differ, both in the elementary layer description (Stroh's formalism for TMM, Helmholtz decomposition for DGM-HD) and in the assembly procedure (propagation of the state vector for TMM, global assembly matrix for DGM-HD).

B. Large fd problem

In Fig. 4, one presents the radial stress response at the receiving point as a function of the normalized frequency $k_e r_0$ for the **RATF0** and **RMTF0** configurations. These configurations do not include any intermediate fluid layer (see Fig. 3(a)). A good agreement between the TMM and DGM-HD calculations is only observed for normalized frequencies below around 100. Above this frequency limit, large singularities between the two calculations can be observed and increase roughly with frequency. This numerical instability can be attributed to the so-called "large fd problem" (Dunkin, 1965; Lévesque and Piché, 1992). It results from the TMM indiscrimination of all exponential partial waves within the layer in the case of a large thickness-frequency combination (Lowe, 1995). For underwater applications considering layers of acoustic materials of several centimeters and a large frequency band of interest, the TMM approach is then not clearly appropriate as highlighted by the results of Figure 4.

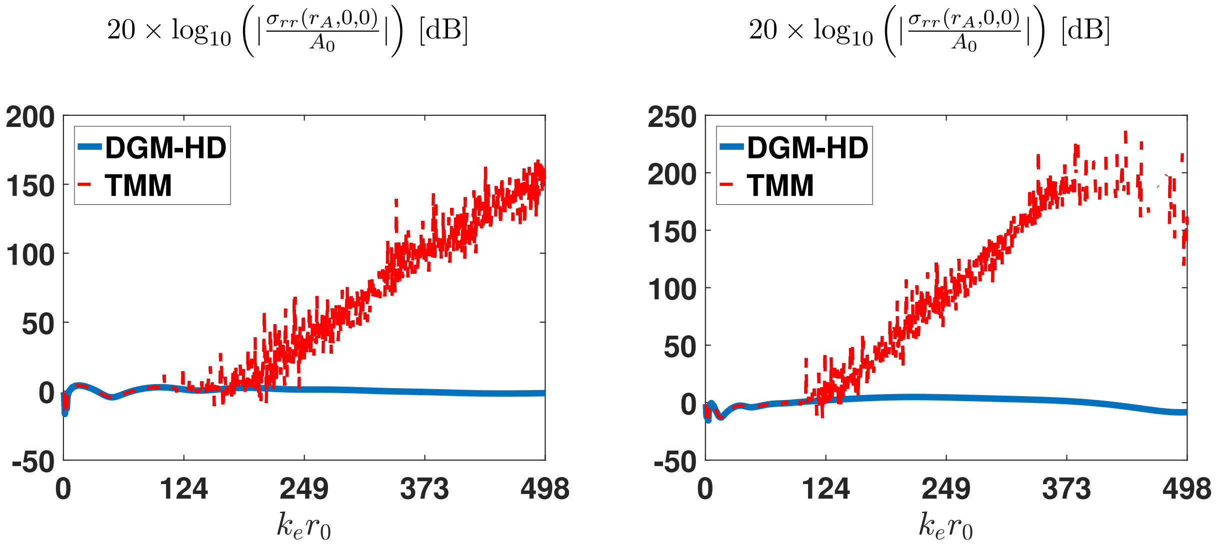

(a) **RATF0** configuration (b) **RMTF0** configuration

FIG. 4. Highlighting instability known as the *large fd problem*: Radial stress at the receiving point for a incident plane wave.

C. Cases with intermediate fluid layers

Now, let us focus on the **RATD0** and **RMTD0** configurations which exhibit an intermediate fluid layer between the PU and GRP layer. As stated previously, the incompatibility of the state vectors between a solid layer and a fluid layer requires a specific treatment in the TMM approach. Two approaches are studied numerically in this subsection, namely the condensation of the solid matrices as presented in the section II E 2 and the introduction of a transverse velocity for mimicking a viscous fluid.

1. Condensation of the solid matrices

The results of the TMM approach using the condensation of the transfer matrices of the solid layers (see section II E 2) are compared in Fig.5 with the DGM-HD results for the two configurations presenting an intermediate fluid layer.

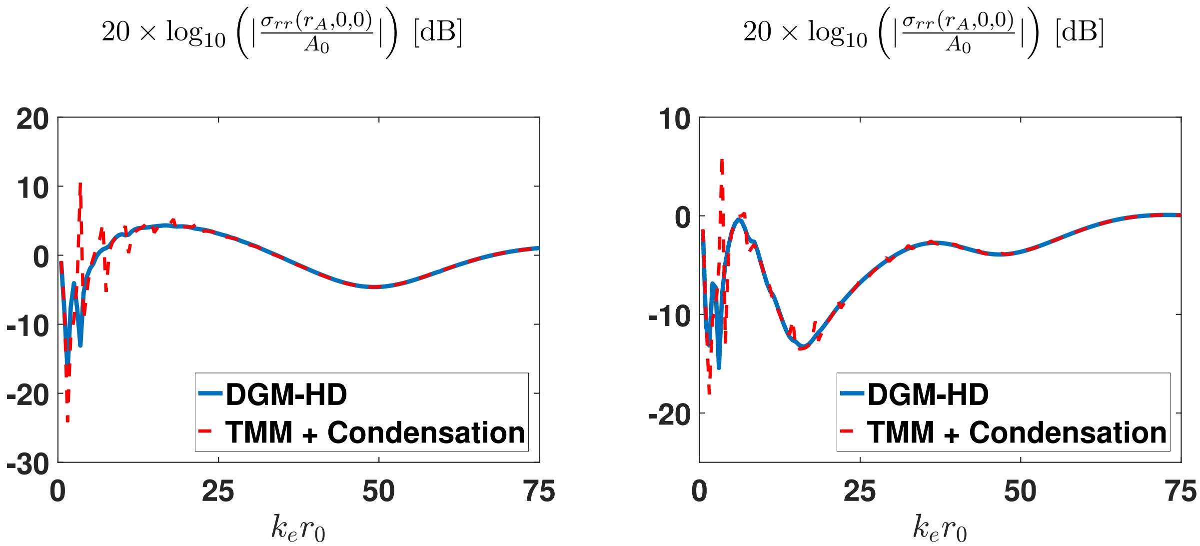

(a) **RATD0** configuration (b) **RMTD0** configuration

FIG. 5. Highlighting the numerical instability in the low frequency domain when using the condensation of the solid transfer matrices: Radial stress at the receiving point for a normal incident plane wave.

These comparisons are performed at low normalized frequencies (i.e. $k_e r_0 < 75$) for which the TMM approach gave satisfactory results for configurations without intermediate fluid layer as shown in Fig. 4. One can observe significant singularities at the lower part of the considered frequency band. This results from the poor conditioning of the matrix inverted in the condensation procedure and the propagation of numerical errors with the classical assembly procedure of the TMM approach.

2. Fluid layers with transverse velocities

Instead of using the condensation procedure, the fluid layer is represented by an isotropic solid layer for which the longitudinal velocity C_L corresponds to the acoustic velocity and the transverse velocity C_T is ”small” but not null. This allows to prevent the inconsistency of the matrix product between a solid layer and a fluid layer. This approach is easy to implement but its difficulty lies in the choice of the transverse velocity. The results of the TMM approach with two different values of the transverse velocity are compared in Fig. 6 with the DGM-HD results used as reference. One can observe that the TMM results depend highly on the values of the transverse velocity loss factor. For $C_T = 1$ m.s^{-1} with a loss factor $\eta_T = 0.05$, the TMM results diverge for normalised frequencies above around 25. On the contrary, a good agreement is observed when $C_T = 1$ m.s^{-1} without damping. However, this last encouraging result obtained for a normal incident plane wave is not general. For instance, for an incident angle of 45°, one can notice in Fig. 6 that the TMM results oscillate around the reference results and the singularities become significant in the higher part of the frequency range. Clearly, this approach for taking the intermediate fluid layer into account is not optimal. It appears difficult to establish a reliable criterion for choosing these parameters, since the two different sets of parameters considered here show very different results, and no good correlation is guaranteed for a wide frequency range and various incident angles.

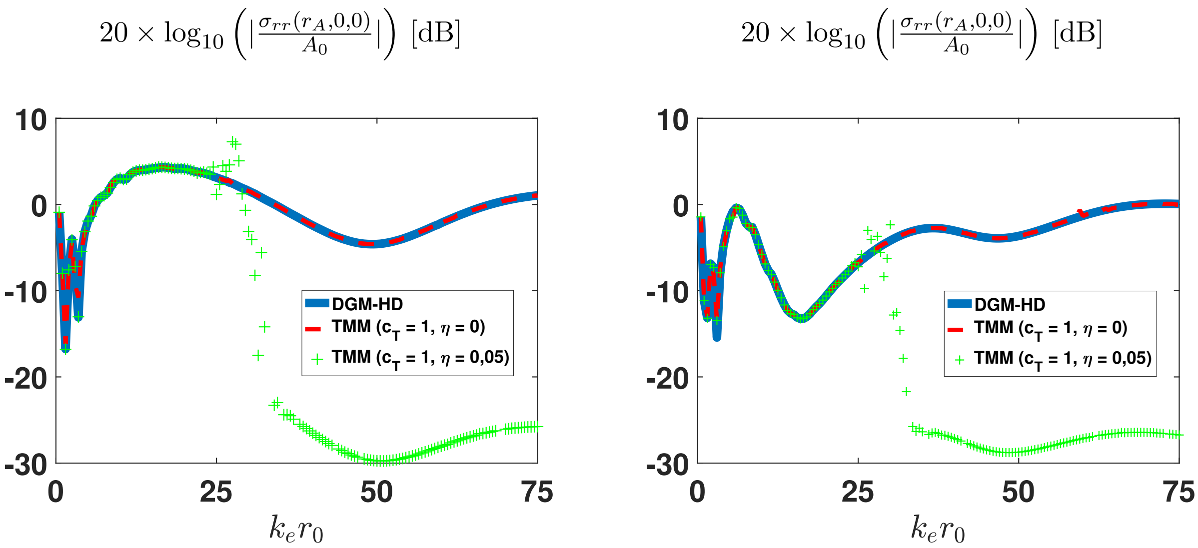

(a) **RATD0** configuration

(b) **RMTD0** configuration

FIG. 6. Highlighting of the responses obtained with the TMM approach when the intermediate fluid layer is represented by an isotropic layer with a small transverse velocity: Radial stress at the receiving point for a normal incident plane wave.

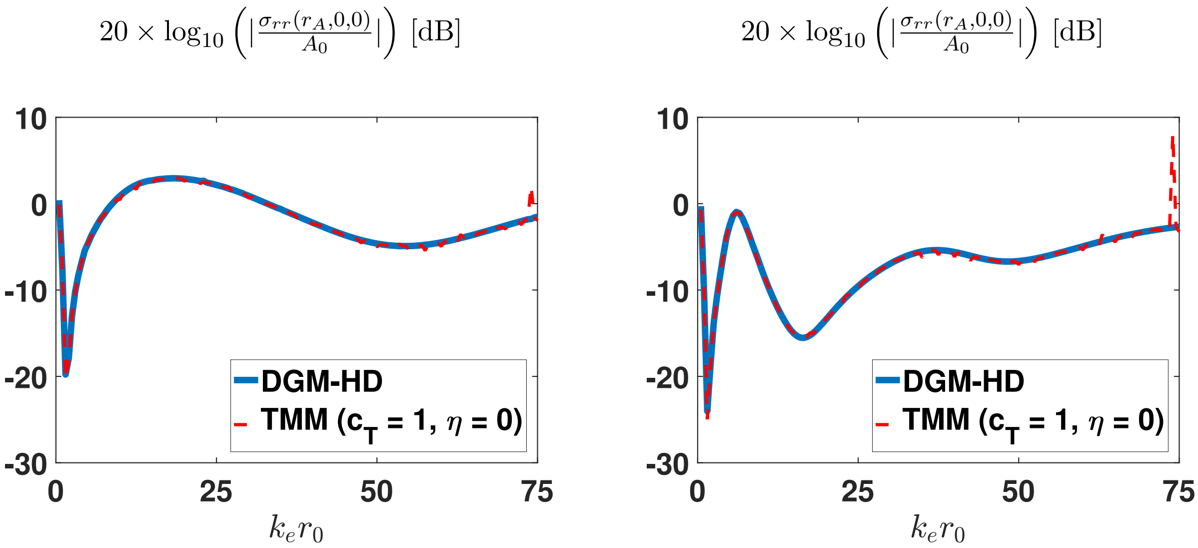

(a) **RATD0** configuration

(b) **RMTD0** configuration

FIG. 7. As the previous figure but for an incident angle of 45°.

IV. SOLVING THE NUMERICAL INSTABILITIES WITH THE PROPOSED ASSEMBLY PROCEDURE

To solve the numerical instabilities related to the "large fd problem" and to overcome the difficulty for the TMM approach to take into account intermediate fluid layers, we propose an alternative approach for assembling the transfer matrix. This procedure is based on building a global matrix similar to the one built in the Dynamic Global Method (DGM) which uses the Helmholtz decomposition in elementary layers (Ricks and Schmidt, 1994). As the transfer matrices of the different layers will be extracted from the Stroh's formalism (as presented in Sec. 2) and the assembly approach will mimic the DGM, we will refer to it as the DGM-SF method in the following whereas DGM-HD will always denote the classical Dynamic Global Method(DGM) using the Helmholtz decomposition in each layer.

The proposed assembly approach is based on the writing in the spectral domain of a global matrix $[\boldsymbol{G}]_{\text{DGM-SF}}(n,\alpha)$ which relates the second member vector $\boldsymbol{E}(n,\alpha)$ characterizing the excitation and a global vector $\{\boldsymbol{V}\}_{\text{GLOB}}(n,\alpha)$ containing all the state vectors evaluated at every lower interface of each layer of the structure:

$$[\boldsymbol{G}]_{\text{DGM-SF}}(n,\alpha)\{\boldsymbol{V}\}_{\text{GLOB}}(n,\alpha) = \boldsymbol{E}(n,\alpha) \tag{36}$$

In the following, we are going to describe how the global matrix $[\boldsymbol{G}]_{\text{DGM-SF}}$ should be built so that the continuity relations on the displacement and stress fields are fulfilled for every interface of the MCS. This assembly procedure depends on the type of interface, and is detailed in the different subsections.

The principle consists in rewriting the continuity relations such that they relate the state vectors at the lower radius of the two layers sharing the considered interface. It permits to deduce the blocks of the global matrix $[\boldsymbol{G}]_{\text{DGM-SF}}$ related to the concatenated subvector composed of state vectors at the lower radius of the layers that share the considered interface.

A. Continuity relations at internal interfaces

1. *Interface between two solid layers*

Let consider the $j+1^{\text{th}}$ interface ($j \in [\![2; \mathrm{N}-1]\!]$) of the structure, separating j^{th} and $j+1^{\text{th}}$ elastic solid layers and having for equation $r = r_j$. The displacement and stress fields are continuous across this interface as it can be described by Eq. (15). Using this equation with Eq. (14), one can relate both state vectors at the bottom of j^{th} and $j+1^{\text{th}}$ layers via the transfer matrix of j^{th} layer:

$$\boldsymbol{V}_{j+1}(r_j, n, \alpha) = [\boldsymbol{T}]_j \, \boldsymbol{V}_j(r_{j-1}, n, \alpha) \tag{37}$$

For convenience, this equation can be rewritten on the form:

$$\begin{pmatrix} [\boldsymbol{T}]_j & -[\boldsymbol{I}_{6\times 6}] \end{pmatrix} \begin{pmatrix} \boldsymbol{V}_j(r_{j-1}, n, \alpha) \\ \\ \boldsymbol{V}_{j+1}(r_j, n, \alpha) \end{pmatrix} = \begin{pmatrix} \boldsymbol{0}_{6\times 1} \\ \\ \boldsymbol{0}_{6\times 1} \end{pmatrix} \tag{38}$$

This equation that expresses the continuity conditions at the interface between the two solid layers is used in practice for filling the global matrix during the assembly procedure as represented in Fig. 8:

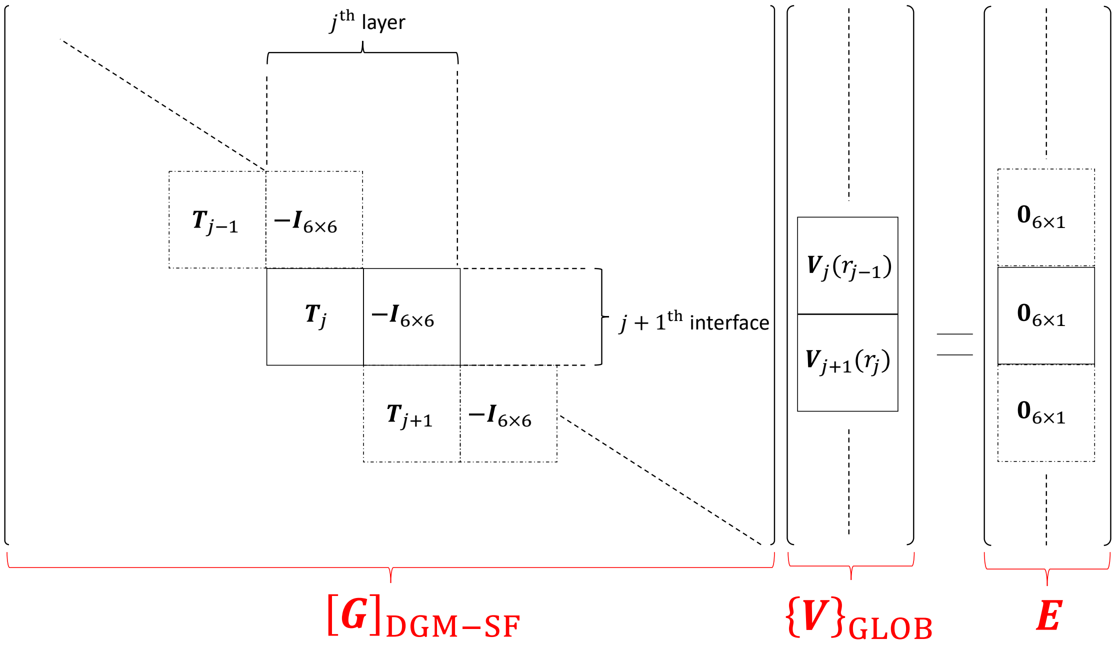

FIG. 8. Global matrix assembly procedure for *solid-solid* interfaces

2. Interface between a solid and a fluid layer

Let consider now an intermediate fluid layer j between two elastic solid layers $j-1$ and $j+1$, then only the normal displacement and the normal stress are continuous across both extremal interfaces of j^{th} layer shared with layers $j-1$ and $j+1$. Since $\boldsymbol{V}_{j-1}$ and $\boldsymbol{V}_{j+1}$ are 6×1 vectors both larger than the 2×1 state vector $\boldsymbol{V}_j$ in the j^{th} layer, one is brought to refer to specific rows of $\boldsymbol{V}_{j-1}$, $\boldsymbol{V}_{j+1}$, and of the transfer matrices of layers $j-1$ and $j+1$ in order to write the continuity relations. The exponents $[3;4]$ make reference to the normal displacement and normal stress (i.e. u_r, σ_{rr}) whereas the exponents $[5;6]$ make reference to the tangential stresses (i.e. $\sigma_{r\phi}$, σ_{rz}).

The continuity relations can then be written:

- for the $j-1^{\mathrm{th}}$ interface:

$$\begin{cases} \boldsymbol{V}_j(r_{j-1},n,\alpha) = \left[\boldsymbol{T}^{[3;4]}\right]_{j-1} \boldsymbol{V}_{j-1}(r_{j-2},n,\alpha) \\ \boldsymbol{V}_{j-1}^{[5;6]}(r_{j-1},n,\alpha) = \left[\boldsymbol{T}^{[5;6]}\right]_{j-1} \boldsymbol{V}_{j-1}(r_{j-2},n,\alpha) = \boldsymbol{0}_{2\times1} \end{cases} \tag{39}$$

- for the j^{th} interface:

$$\begin{cases} \boldsymbol{V}_{j+1}^{[3;4]}(r_j,n,\alpha) = \boldsymbol{V}_j(r_j,n,\alpha) = \left[\boldsymbol{T}\right]_j \boldsymbol{V}_j(r_{j-1},n,\alpha) \\ \boldsymbol{V}_{j+1}^{[5;6]}(r_j,n,\alpha) = \boldsymbol{0}_{2\times1} \end{cases} \tag{40}$$

where exponents $[3;4]$ and $[5;6]$ remind the corresponding rows in state vectors of the considered solid layers.

This set of 8 equations can rewritten on the following form:

$$\begin{pmatrix} \left[\boldsymbol{T}^{[3;4]}\right]_{j-1} & -\left[\boldsymbol{I}_{2\times2}\right] \\ \left[\boldsymbol{T}^{[5;6]}\right]_{j-1} & \left[\boldsymbol{0}_{2\times2}\right] \end{pmatrix} \begin{pmatrix} \boldsymbol{V}_{j-1}(r_{j-2},n,\alpha) \\ \boldsymbol{V}_j(r_{j-1},n,\alpha) \end{pmatrix} = \begin{pmatrix} \boldsymbol{0}_{2\times1} \\ \boldsymbol{0}_{2\times1} \end{pmatrix} \tag{41}$$

$$\begin{pmatrix} \left[\boldsymbol{T}\right]_j & \left[\ \left[\boldsymbol{0}_{2\times2}\right] \ -\left[\boldsymbol{I}_{2\times2}\right] \ \left[\boldsymbol{0}_{2\times2}\right]\ \right] \\ \left[\boldsymbol{0}_{2\times2}\right] & \left[\ \left[\boldsymbol{0}_{2\times2}\right] \ \left[\boldsymbol{0}_{2\times2}\right] \ \left[\boldsymbol{I}_{2\times2}\right]\ \right] \end{pmatrix} \begin{pmatrix} \boldsymbol{V}_j(r_{j-1},n,\alpha) \\ \boldsymbol{V}_{j+1}(r_j,n,\alpha) \end{pmatrix} = \begin{pmatrix} \boldsymbol{0}_{2\times1} \\ \boldsymbol{0}_{2\times1} \end{pmatrix} \tag{42}$$

Once again, these equations are used to fill the global matrix by blocks as represented in Fig. 9.

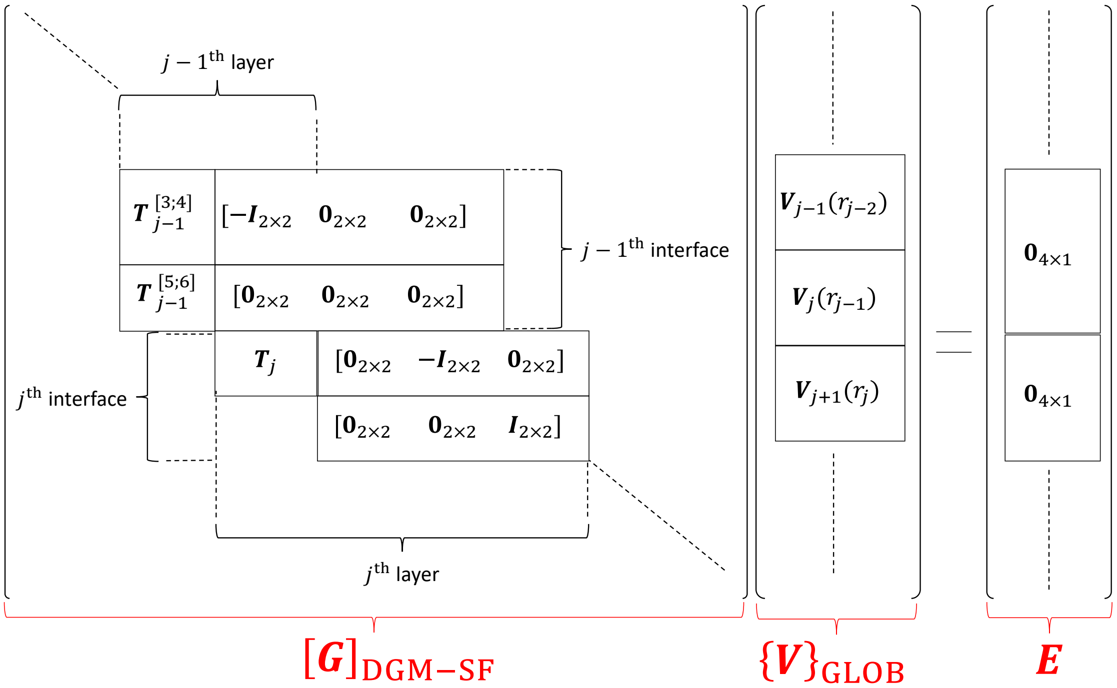

FIG. 9. Global matrix assembly procedure for *solid-fluid* interfaces

3. *Continuity relations at extremal interfaces*

The continuity relations at both internal and extremal radiuses provide 6 equations in total, which take the following form in the case of the plane wave excitation:

$$
\begin{aligned}
\boldsymbol{V}_1^{[4;6]}(r_0,n,\alpha) &= \begin{bmatrix} [\boldsymbol{T}_{\mathrm{fi}}] & [\mathbf{0}_{3\times3}] \end{bmatrix} \boldsymbol{V}_1(r_0,n,\alpha) \\
\boldsymbol{V}_{\mathrm{N}}^{[4;6]}(r_{\mathrm{N}},n,\alpha) &= -\boldsymbol{P}_{\mathrm{b}}(r_{\mathrm{N}},n,\alpha) - \begin{bmatrix} [\boldsymbol{T}_{\mathrm{fe}}] & [\mathbf{0}_{3\times3}] \end{bmatrix} \boldsymbol{V}_{\mathrm{N}}(r_{\mathrm{N}},n,\alpha)
\end{aligned}
\qquad (43)
$$

where the $\boldsymbol{P}_{\mathrm{b}}$ vector and the $[\boldsymbol{T}_{\mathrm{fi}}]$, $[\boldsymbol{T}_{\mathrm{fe}}]$ matrices have been defined in section II F. These equations can be rewritten on the form:

$$
\begin{bmatrix} -[\boldsymbol{T}_{\mathrm{fi}}] & [\boldsymbol{I}_{3\times3}] \end{bmatrix} \boldsymbol{V}_1(r_0,n,\alpha) = \mathbf{0}_3 \qquad (44)
$$

$$\begin{bmatrix} [\boldsymbol{T}_{\text{fe}}] & [\boldsymbol{I}_{3\times3}] \end{bmatrix} \boldsymbol{V}_{\text{N}}(r_{\text{N}}, n, \alpha) = -\boldsymbol{P}_{\text{b}}(r_{\text{N}}, n, \alpha) \tag{45}$$

However, the state vector at the top of the last layer $\boldsymbol{V}_{\text{N}}(r_{\text{N}}, n, \alpha)$ is not stored in the global vector $\{\boldsymbol{V}\}_{\text{GLOB}}$. Hence, Eq. (45) is rewritten in function of state vector at the bottom of the last layer $\boldsymbol{V}_{\text{N}}(r_{\text{N-1}}, n, \alpha)$ by using the transfer matrix of the last layer $[\boldsymbol{T}_{\text{N}}]$:

$$\begin{bmatrix} [\boldsymbol{T}_{\text{fe}}] & [\boldsymbol{I}_{3\times3}] \end{bmatrix} [\boldsymbol{T}_{\text{N}}]\, \boldsymbol{V}_{\text{N}}(r_{\text{N}-1}, n, \alpha) = -\boldsymbol{P}_{\text{b}}(r_{\text{N}}, n, \alpha) \tag{46}$$

The equations 44 and 46 are used to fill by blocks the global matrix as represented in Fig. 10.

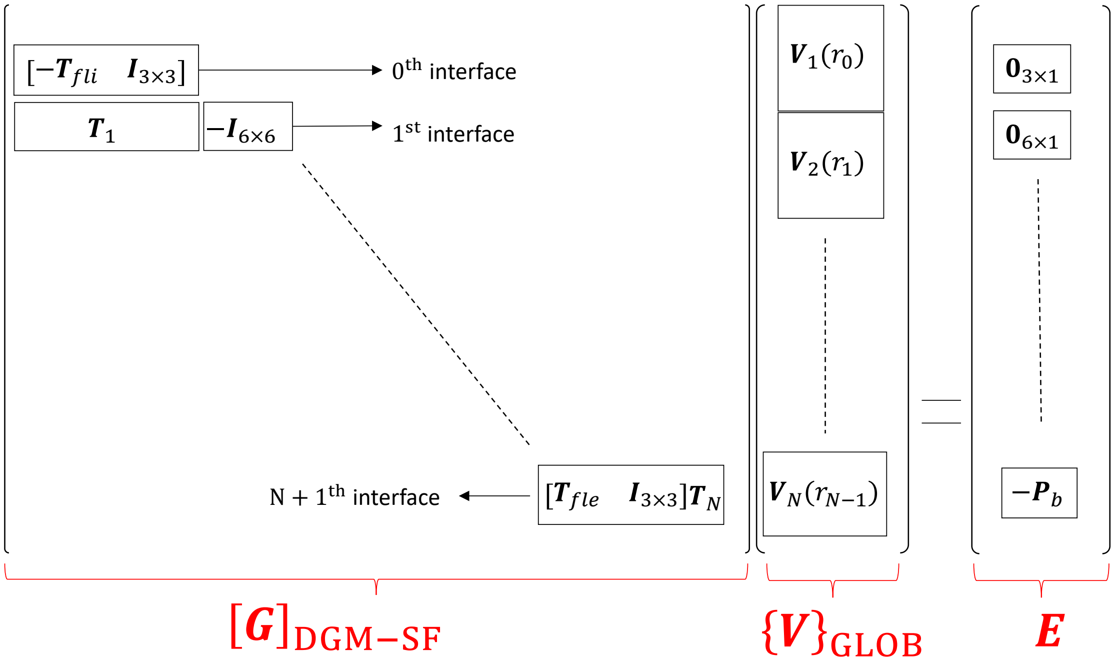

FIG. 10. Global matrix assembly procedure for extremal interfaces.

4. Summarize

The DGM-SF procedure can be decomposed in three steps:

- the transfer matrix of each layer (or each sublayer) is estimated accordingly to the developments of the section 2.4;
- the global matrix $\{\boldsymbol{V}\}_{\text{GLOB}}(n, \alpha)$ and the second member vector $\boldsymbol{E}(n, \alpha)$ are filled by blocks depending on the type of layer (or sublayer) interface as summarized by Figures 7, 8 and 9;
- the global matrix system (36) is solved. The state vector at the bottom of the layer containing the receiving point, is then propagated to the radius of the receiving point using the transfer matrix between the internal radius and the radius of the receiving point. The response at the receiving point is then deduced from the inverse Fourier transforms (3) of the state vector in the wavenumber domain (n, α).

B. Numerical stability enhancement provided by the DGM-SF

In this section, we highlight the numerical stability improvements provided by the proposed assembly procedure, both on the "large fd problem" and the ability to take into account intermediate fluid layers.

1. About the "large fd problem"

Figure 11 represents the modulus of the spectral radial displacement at the inner radius of the steel shell in the normalized frequency-circumferential order $(k_e r_0, n)$ space for the **RMTF0** configuration. The results obtained by the two assembly procedures are compared. One notices a good agreement between the two calculations only for both the low circumferential orders and the low frequency of the considered frequency range. Outside this domain, the conventional TMM assembly procedure exhibits results that are noisy and largely different from those of the proposed DGM-SF assembly procedure. For validation, the latter compared with the DGM-HD reference results on Figure 12 for both **RATF0** and **RMTF0** configurations. One recalls that the TMM approach gave poor results on Figure 4 for the same configurations. A very good agreement can be observed on Figure 12 between the DGM-HD et DGM-SF calculations, even for the highest part of the frequency range of interest. Other comparisons (not presented here) for different incident angles of the acoustic waves show also a good agreement between DGM-HD et DGM-SF. This shows that the DGM-SF procedure allows to overcome the numerical instability of the TMM assembly procedure related to the "large fd problem".

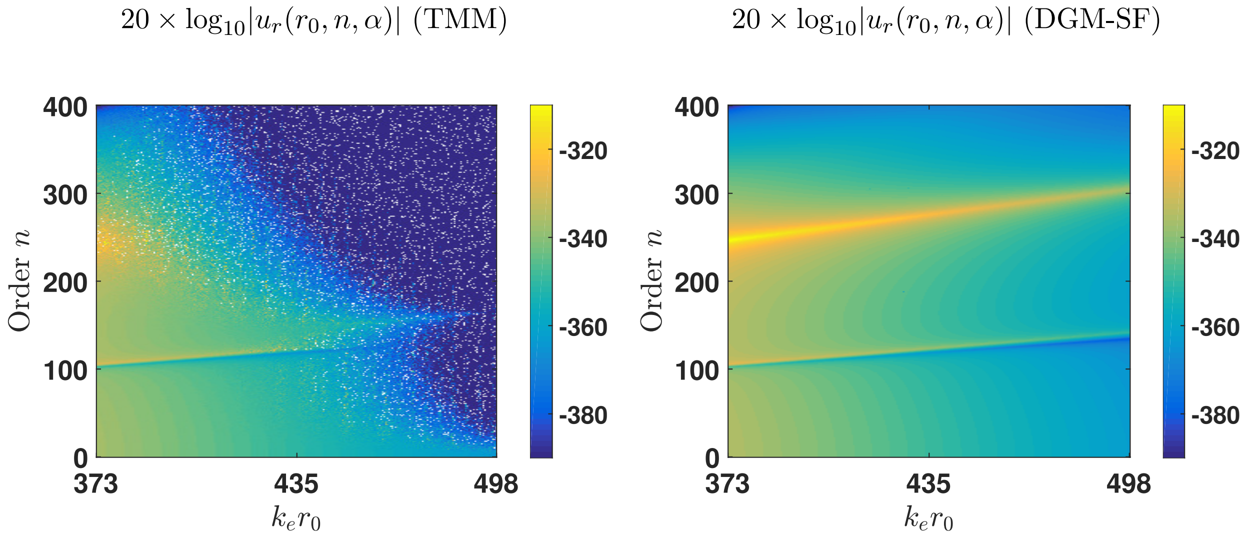

(a) TMM approach

(b) DGM-SF approach

FIG. 11. Comparison of the spectral displacements at the inner radius calculated by the TMM and DGM-SF approaches for the **RMTF0** configuration.

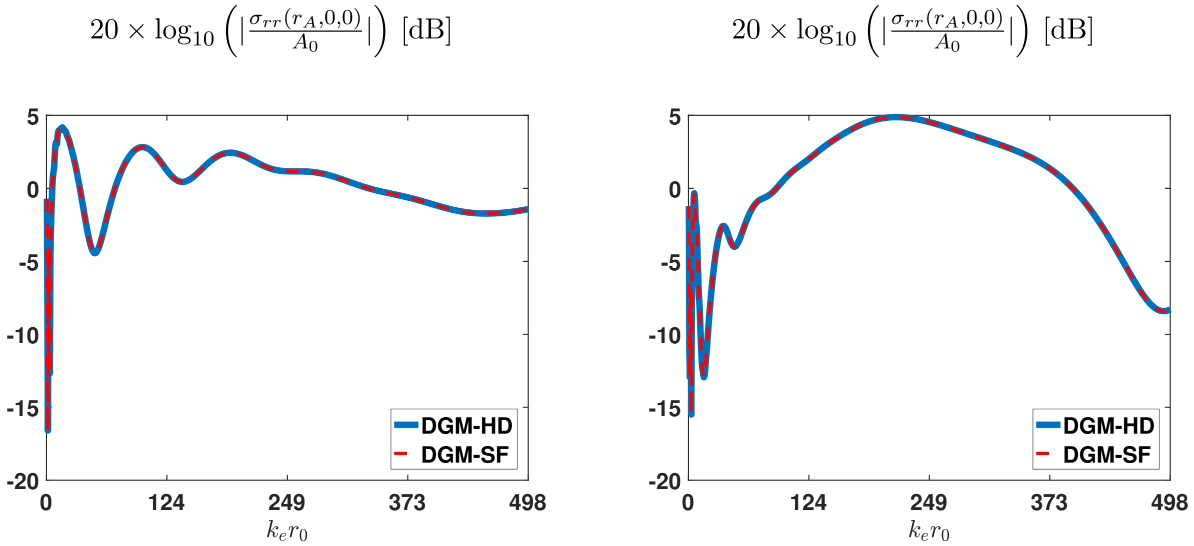

(a) **RATF0** configuration (b) **RMTF0** configuration

FIG. 12. Validation of DGM-SF assembly procedure for the cases without intermediate fluid layers. Radial stress at the receiving point for a normal incident plane wave.

2. *About the difficulty of taking into account intermediate fluid layers*

In this section, one highlights the ability of the DGM-SF assembly procedure to take into account intermediate fluid layers. As seen earlier on Fig. 5 and Fig. 6, classical TMM assembly procedure is not well suited to describe intermediate fluid layers, and very poor correlation can be noted at low frequency regime with the DGM-HD reference model, either when condensating transfer matrices of solid layers or when introducing low transverse velocities into intermediate fluid layers.

The comparison of DGM-HD and DGM-SF results is proposed in Fig. 13 for **RATD0** and **RMTD0** configurations which both exhibit an intermediate fluid layer. Again, one can notice a good agreement between the two approaches.

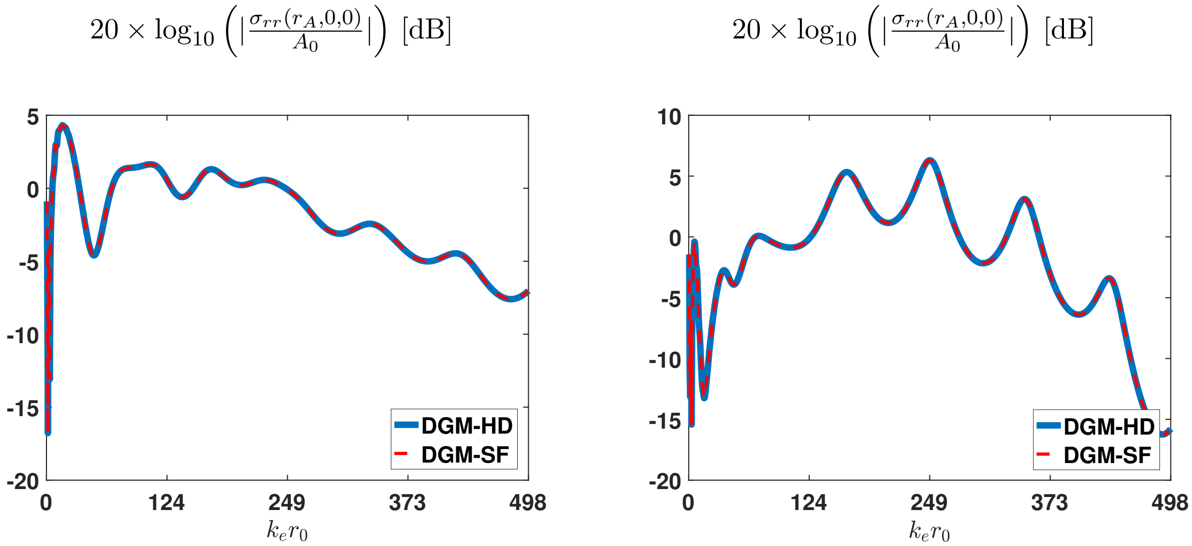

(a) Configuration **RATD0** (b) Configuration **RMTD0**

FIG. 13. Validation of DGM-SF assembly procedure for the cases with an intermediate fluid layer. Radial stress at the receiving point for a normal incident plane wave.

V. ABILITY OF THE PROPOSED DGM-SF PROCEDURE TO MODEL THE ANISOTROPY OF SOLID LAYERS

Before concluding, we illustrate on an application case the interest of the DGM-SF approach compared to the DGM-HD one. Unlike the DGM-HD method that performs a Helmholtz decomposition in each elementary solid layer assuming particular material symmetries (as isotropic), the proposed DGM-SF procedure integrates the Stroh's first-order differential system without making any assumptions on the material symmetries (see section 2).

For underwater applications, the GRP layer that may represent an acoustic dome of a Sonar flank array and that has been considered in the **RATD0** and **RMTD0** configurations is typically an anisotropic layer. As the GRP material can be manufactured by adding layers of woven roving and resin, the mechanical properties are different in the fiber plane from transversely to the plane. For the considered cylindrical GRP layer, one can suppose that the woven rovings are rolled around a cylinder with different directions of the fibers for each roving. It results that the fibers are randomly oriented in the plane $(\boldsymbol{e}_\phi, \boldsymbol{e}_z)$. The GRP is thus well represented by a transversely isotropic model, and Young moduli in the directions of the fibers (i.e. $(\boldsymbol{e}_\phi, \boldsymbol{e}_z)$) are higher than the transverse Young modulus (i.e. in the radial direction $\boldsymbol{e}_r$).

To illustrate the effect of this anisotropy, one has started from the characteristics of the supposed isotropic GRP layer defined in Table I and one has modified the Young modulus in the $\boldsymbol{e}_r$ direction to define one transverse isotropic configuration as presented in Table II. A distinction of the material properties has been made between the radial direction numbered 1 and those of the fiber "plane" numbered 2 and 3. The Young's modulus in the radial direction has been softened by imposing the value of $\frac{E_2}{E_1}$ ratio, where GRP 3/1 stands for $\frac{E_2}{E_1} = 3$. These characteristics are used to calculate the stiffness constants of the Hooke law (defined with Eq. (47)) and then the Stroh's matrix with Eq. (5). The integration of the Stroh's differential system can be achieved as described in the section II D 1 in order to deduce the transfer matrix of the transverse isotropic GRP layer. The radial stress responses at the receiving point have been compared for the **RATD0** and **RMTD0** configurations considering both isotropic and transverse isotropic GRP cases defined in Table II. Fig. 14 shows the radial stress responses at the receiving point r_A for both **RATD0** and **RMTD0**

TABLE II.

Mechanical properties, isotropic (GRP ISO) versus transverse isotropic case (GRP 3/1).

	GRP ISO	GRP 3/1
E_1 (GPa)	$17,7$	$6,00$
$E_2 = E_3$ (GPa)	$17,7$	$17,7$
$G_{12} = G_{13}$ (GPa)	$7,92$	$3,00$
G_{23} (GPa)	$7,92$	$7,92$
$\nu_{12} = \nu_{13}$	$0,2$	$0,2$
ν_{23}	$0,1$	$0,1$
ρ (kg.m^{-3})	2000	2000

configurations. On top are represented the responses for normal incidence, and below those for an oblique incidence of (45°) of the acoustic wave.

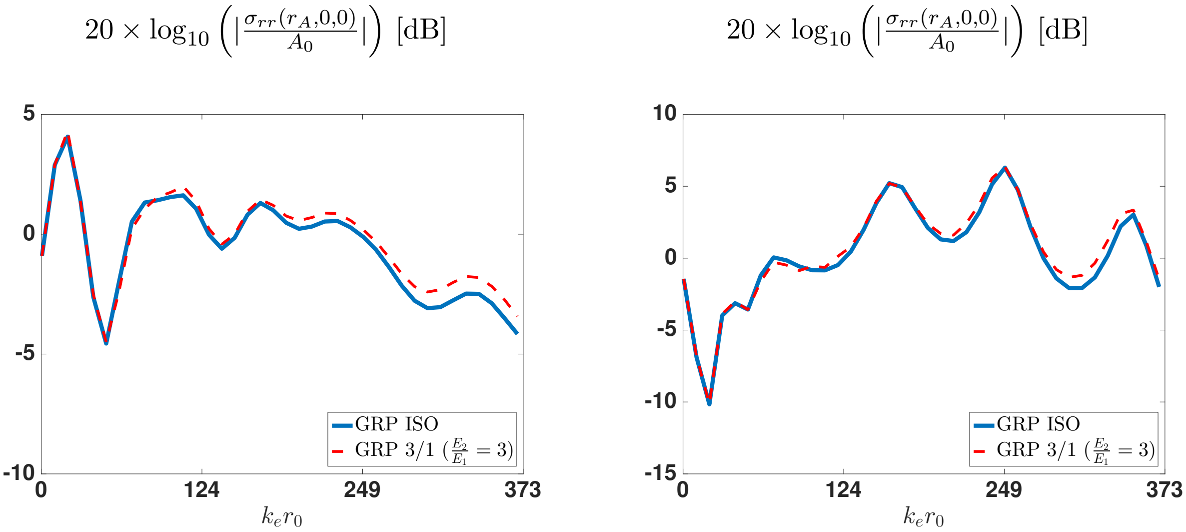

(a) Configuration **RATD0**, normal incidence (b) Configuration **RMTD0**, normal incidence

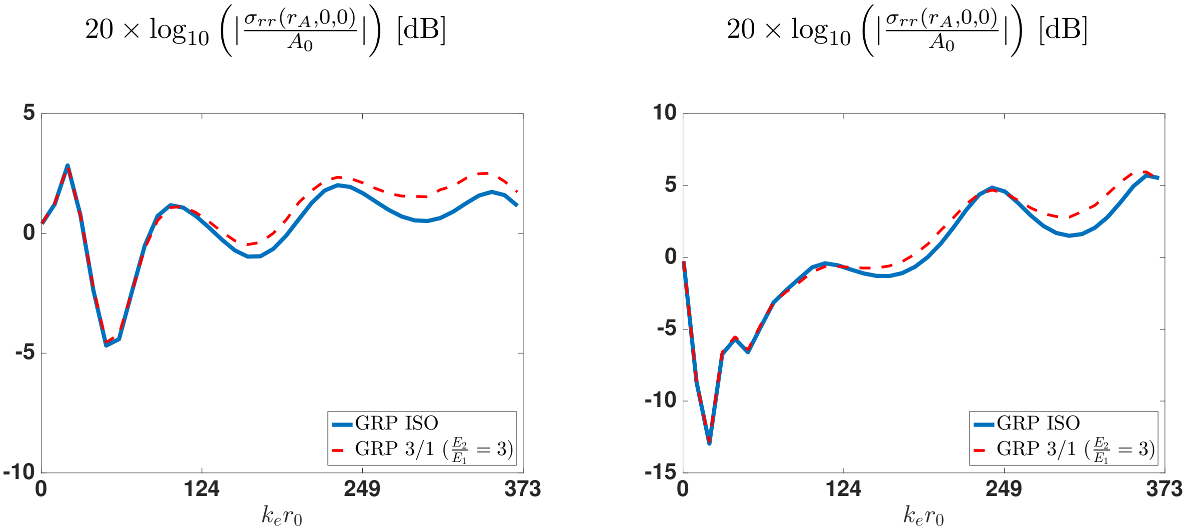

(c) Configuration **RATD0**, oblique incidence (45°) (d) Configuration **RMTD0**, oblique incidence ($45^{c}irc$)

FIG. 14. Influence of the transverse isotropic model for the GRP layer: Radial stress at the receiving point for normal and oblique (45°) incident plane wave.

556 Differences are observed on each excitation case between both GRP models at high frequencies. Larger differences are observed for **RATD0** configuration at both incidences. For the higher frequencies of the considered frequency range, one can notice that the re-

sponses obtained with the transverse anisotropic GRP model have greater levels than with the isotropic GRP model. This is explained by the fact that the Young modulus has been softened in the transverse anisotropic model, increasing the transmission coefficient of the GRP, and increasing the level at the sensor radius.

This result allows us illustrating the interest of the DGM-SF approach. It should however not be considered as a general statement. A detailed study should be carried out in the future to understand the effect of transverse isotropic layer on the response of a multilayered cylindrical shell impacted by a plane wave. It is however outside the scope of the present paper.

VI. CONCLUSION

A semi-analytical model of a multilayered cylindrical shell immersed in water and excited by an acoustic plane wave has been developed for underwater applications. One has shown that the classical transfer matrix method (TMM) allowing to assembly the transfer matrix of each layer lead to numerical instabilities. These have been highlighted on typical underwater configurations. The first instability is related to the well-known "large fd problem" whereas the second one is induced by the matrix condensation used to take into account intermediate fluid layers. An alternative assembly procedure based on the building of a global matrix has been proposed to overcome these instabilities. It leads to the DGM-SF approach that allows us to describe each solid layer with the Stroh's formalism and to assemble them by a global matrix. It results in an efficient and numerical stable process that has been validated on different underwater configurations. Moreover, the process is well suited to take into account anisotropic layers such as composite acoustic windows.

ACKNOWLEDGMENTS

This work was performed within the framework of the LABEX CeLyA (ANR-10-LABX-0060) of Université de Lyon, within the program "Investissements d'Avenir" (ANR-16-IDEX-0005) operated by the French National Research Agency (ANR).

APPENDIX: STROH'S OPERATOR FOR AN ORTHOTROPIC LAYER

For an orthotropic layer, the Hooke's law can be written as:

$$\begin{pmatrix} \sigma_{rr} \\ \sigma_{\phi\phi} \\ \sigma_{zz} \\ \sigma_{\phi z} \\ \sigma_{rz} \\ \sigma_{r\phi} \end{pmatrix} = \begin{bmatrix} c_{11} & c_{12} & c_{13} & 0 & 0 & 0 \\ c_{12} & c_{22} & c_{23} & 0 & 0 & 0 \\ c_{13} & c_{23} & c_{33} & 0 & 0 & 0 \\ 0 & 0 & 0 & c_{44} & 0 & 0 \\ 0 & 0 & 0 & 0 & c_{55} & 0 \\ 0 & 0 & 0 & 0 & 0 & c_{66} \end{bmatrix} \begin{pmatrix} \epsilon_{rr} \\ \epsilon_{\phi\phi} \\ \epsilon_{zz} \\ \gamma_{\phi z} \\ \gamma_{rz} \\ \gamma_{r\phi} \end{pmatrix} \tag{47}$$

where c_{ij} are the elastic constants.

The Stroh's operator can then be written:

$$[\boldsymbol{\mathfrak{Q}}] = \begin{bmatrix} 0 & 0 & -\dfrac{\partial}{\partial z} & 0 & 0 & \dfrac{1}{c_{55}} \\[2ex] 0 & \dfrac{1}{r} & -\dfrac{1}{r}\dfrac{\partial}{\partial \theta} & 0 & \dfrac{1}{c_{66}} & 0 \\[2ex] -\dfrac{c_{13}}{c_{11}}\dfrac{\partial}{\partial z} & -\dfrac{c_{12}}{c_{11}r}\dfrac{\partial}{\partial \theta} & -\dfrac{c_{12}}{c_{11}r} & \dfrac{1}{c_{11}} & 0 & 0 \\[2ex] \dfrac{e_{23}}{r}\dfrac{\partial}{\partial z} & \dfrac{e_{22}}{r^2}\dfrac{\partial}{\partial \theta} & \dfrac{e_{22}}{r^2} - \rho\omega^2 & \dfrac{1}{r}\left(\dfrac{c_{12}}{c_{11}} - 1\right) & -\dfrac{1}{r}\dfrac{\partial}{\partial \theta} & -\dfrac{\partial}{\partial z} \\[2ex] -\dfrac{1}{r}\left(c_{44} + e_{23}\right)\dfrac{\partial^2}{\partial \theta \partial z} & -\left[\rho\omega^2 + \dfrac{e_{22}}{r^2}\dfrac{\partial^2}{\partial \theta^2} + c_{44}\dfrac{\partial^2}{\partial z^2}\right] & -\dfrac{e_{22}}{r^2}\dfrac{\partial}{\partial \theta} & -\dfrac{c_{12}}{c_{11}r}\dfrac{\partial}{\partial \theta} & -\dfrac{2}{r} & 0 \\[2ex] -\left[\rho\omega^2 + \dfrac{c_{44}}{r^2}\dfrac{\partial^2}{\partial \theta^2} + e_{33}\dfrac{\partial^2}{\partial z^2}\right] & -\dfrac{1}{r}\left(c_{44} + e_{23}\right)\dfrac{\partial^2}{\partial \theta \partial z} & -\dfrac{e_{23}}{r}\dfrac{\partial}{\partial z} & -\dfrac{c_{13}}{c_{11}}\dfrac{\partial}{\partial z} & 0 & -\dfrac{1}{r} \end{bmatrix} \tag{48}$$

where ρ is the mass density of the considered layer and e_{ij} are derived from the elastic constants c_{ij}:

$$e_{22} = \left(c_{22} - \frac{c_{12}^2}{c_{11}}\right), e_{23} = \left(c_{23} - \frac{c_{12}c_{13}}{c_{11}}\right), e_{33} = \left(c_{33} - \frac{c_{13}^2}{c_{11}}\right) \tag{49}$$

Applying the Fourier transform defined by Eq. (4) to the Stroh'operator gives the Stroh matrix:

$$[\boldsymbol{Q}(r)] = \begin{bmatrix} 0 & 0 & -i\alpha & 0 & 0 & \dfrac{1}{c_{55}} \\ 0 & \dfrac{1}{r} & -\dfrac{in}{r} & 0 & \dfrac{1}{c_{66}} & 0 \\ -i\alpha\dfrac{c_{13}}{c_{11}} & -\dfrac{in}{r}\dfrac{c_{12}}{c_{11}} & -\dfrac{c_{12}}{c_{11}r} & \dfrac{1}{c_{11}} & 0 & 0 \\ i\alpha\dfrac{e_{23}}{r} & \dfrac{in}{r^2}e_{22} & \dfrac{e_{22}}{r^2}-\rho\omega^2 & \dfrac{1}{r}\left(\dfrac{c_{12}}{c_{11}}-1\right) & -\dfrac{in}{r} & -i\alpha \\ \alpha\dfrac{n}{r}\left(c_{44}+e_{23}\right) & \dfrac{n^2}{r^2}e_{22}+\alpha^2c_{44}-\rho\omega^2 & -\dfrac{in}{r^2}e_{22} & -\dfrac{in}{r}\dfrac{c_{12}}{c_{11}} & -\dfrac{2}{r} & 0 \\ \dfrac{n^2}{r^2}c_{44}+\alpha^2e_{33}-\rho\omega^2 & \dfrac{\alpha n}{r}\left(c_{44}+e_{23}\right) & -\dfrac{i\alpha}{r}e_{23} & -i\alpha\dfrac{c_{13}}{c_{11}} & 0 & -\dfrac{1}{r} \end{bmatrix} \tag{50}$$

Abramowitz, M., and Stegun, I. (**1965**). *Handbook of mathematical functions: with formulas, graphs, and mathematical tables*, **55** (Courier Corporation).

Baron, C. (**2005**). "Le développement en série de peano du matricant pour l'étude de la propagation des ondes élastiques en milieux à propriétés continûment variables," Ph.D. thesis, Université Sciences et Technologies-Bordeaux I.

Baron, C. (**2011**). "Propagation of elastic waves in an anisotropic functionally graded hollow cylinder in vacuum," Ultrasonics **51**(2), 123–130.

Cervenka, P., and Challande, P. (**1991**). “A new efficient algorithm to compute the exact reflection and transmission factors for plane waves in layered absorbing media (liquids and solids),” The Journal of the Acoustical Society of America **89**(4), 1579–1589.

Chen, W., Bian, Z., and Ding, H. (**2004**). “Three-dimensional vibration analysis of fluid-filled orthotropic fgm cylindrical shells,” International Journal of Mechanical Sciences **46**(1), 159–171.

Dunkin, J. (**1965**). “Computation of modal solutions in layered, elastic media at high frequencies,” Bulletin of the Seismological Society of America **55**(2), 335–358.

Dutrion, C. (**2014**). “Étude de faisabilité d’un revêtement élastique pour la furtivité acoustique.,” Ph.D. thesis, Institut Supérieur de l’Aéronautique et de l’Espace-ISAE.

Hasheminejad, S., and Rajabi, M. (**2007**). “Acoustic scattering characteristics of a thick-walled orthotropic cylindrical shell at oblique incidence,” Ultrasonics **47**(1-4), 32–48.

Honarvar, F., Enjilela, E., Sinclair, A., and Mirnezami, S. (**2007**). “Wave propagation in transversely isotropic cylinders,” International journal of solids and structures **44**(16), 5236–5246.

Hull, A., and Welch, J. (**2010**). “Elastic response of an acoustic coating on a rib-stiffened plate,” Journal of Sound and Vibration **329**, 4192–4211, `http://gen.lib.rus.ec/scimag/index.php?s=10.1016/j.jsv.2010.04.012`, doi: `10.1016/j.jsv.2010.04.012`.

Jamali, J., Naei, M., Honarvar, F., and Rajabi, M. (**2011**). “Acoustic scattering from functionally graded cylindrical shells,” Archives of Mechanics **63**(1), 25–56.

Kim, J.-Y., and Ih, J.-G. (**2003**). “Scattering of plane acoustic waves by a transversely isotropic cylindrical shell—application to material characterization,” Applied Acoustics

64, 1187–1204.

Lévesque, D., and Piché, L. (**1992**). “A robust transfer matrix formulation for the ultrasonic response of multilayered absorbing media,” The Journal of the Acoustical Society of America **92**(1), 452–467.

Lowe, M. (**1995**). “Matrix techniques for modeling ultrasonic waves in multilayered media,” IEEE transactions on ultrasonics, ferroelectrics, and frequency control **42**(4), 525–542.

Maxit, L. (**2014**). “Scattering model of a cylindrical shell with internal axisymmetric frames by using the circumferential admittance approach,” Applied Acoustics **80**, 10–22.

Nayfeh, A., and Taylor, T. (**1988**). “Surface wave characteristics of fluid-loaded multilayered media,” The Journal of the Acoustical Society of America **84**(6), 2187–2191.

Niklasson, A., and Datta, S. (**1998**). “Scattering by an infinite transversely isotropic cylinder in a transversely isotropic medium,” Wave Motion **27**, 169–185.

Pialucha, T. (**1992**). “The reflection coefficient from interface layers in ndt of adhesive joints,” Ph.D. thesis, University of London.

Pilarski, A. (**1985**). “Ultrasonic evaluation of the adhesion degree in layered joints,” Mayrt. Eval. **43**(6), 765–770.

Ricks, D., and Schmidt, H. (**1994**). “A numerically stable global matrix method for cylindrically layered shells excited by ring forces,” The Journal of the Acoustical Society of America **95**(6), 3339–3349.

Rokhlin, S., and Wang, L. (**2002**). “Stable recursive algorithm for elastic wave propagation in layered anisotropic media: Stiffness matrix method,” The Journal of the Acoustical Society of America **112**(3), 822–834.

Schmidt, H., and Jensen, F. (**1985**). “A full wave solution for propagation in multilayered viscoelastic media with application to gaussian beam reflection at fluid–solid interfaces,” The Journal of the Acoustical Society of America **77**(3), 813–825.

Skelton, E., and James, J. (**1997**). *Theoretical acoustics of underwater structures* (World Scientific Publishing Company).

Tan, E. (**2005**). “Stiffness matrix method with improved efficiency for elastic wave propagation in layered anisotropic media,” The Journal of the Acoustical Society of America **118**(6), 3400–3403.